FUNCTION®

american physiological society®

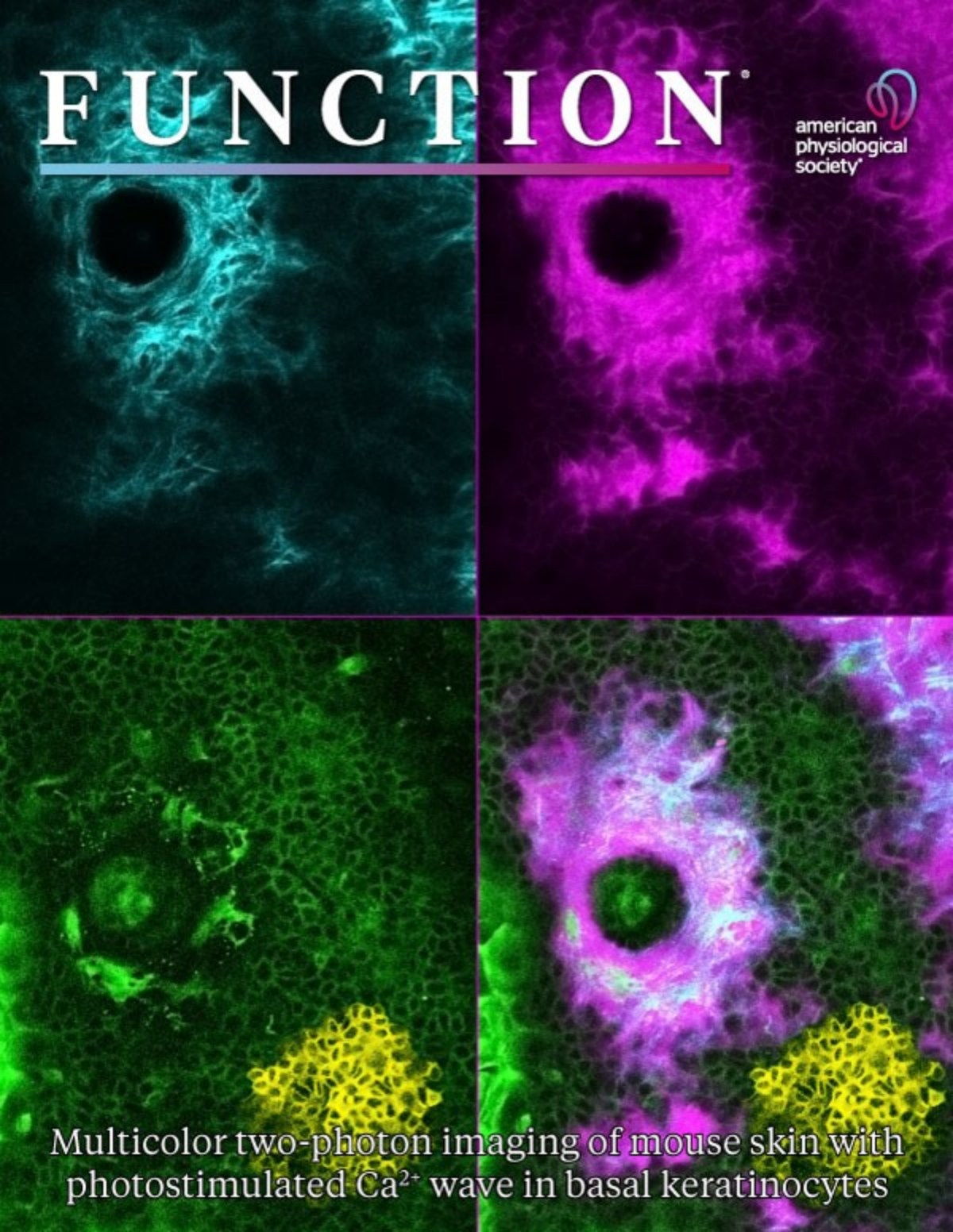

Multicolor two-photon imaging of mouse skin with photostimulated Ca^{2+} wave in basal keratinocytes

FUNCTION™ american physiological society

FUNCTION, 2021, 3(1): zqab064

https://doi.org/10.1093/function/zqab064
Advance Access Publication Date: 1 December 2021
Research Article

RESEARCH ARTICLE

Calcium Signaling in the Photodamaged Skin: In Vivo Experiments and Mathematical Modeling

Viola Donati[1,2,†], Chiara Peres[2,†], Chiara Nardin[2], Ferdinando Scavizzi[2], Marcello Raspa[2], Catalin D. Ciubotaru[3], Mario Bortolozzi[1,2,4,*], Morten Gram Pedersen[5,6,*], Fabio Mammano[1,2,*]

[1]Department of Physics and Astronomy "G. Galilei", University of Padova, 35131 Padova, Italy, [2]Institute of Biochemistry and Cell Biology (IBBC)-CNR, 00015 Monterotondo (RM), Italy, [3]IOM-CNR, Institute of Materials, Area Science, 34149 Basovizza (TS), Italy, [4]Foundation for Advanced Biomedical Research, Veneto Institute of Molecular Medicine (VIMM), 35129 Padova (PD), Italy, [5]Department of Information Engineering, University of Padova, 35131 Padova (PD), Italy and [6]Department of Mathematics "Tullio Levi-Civita", University of Padova, 35121 Padova (PD), Italy

*Address correspondence to F.M. (e-mail: fabio.mammano@unipd.it), M.G.P. (mortengram.pedersen@unipd.it), M.B. (mario.bortolozzi@unipd.it)
†Equal contribution.

Abstract

The epidermis forms an essential barrier against a variety of insults. The overall goal of this study was to shed light not only on the effects of accidental epidermal injury, but also on the mechanisms that support laser skin resurfacing with intra-epidermal focal laser-induced photodamage, a widespread medical practice used to treat a range of skin conditions. To this end, we selectively photodamaged a single keratinocyte with intense, focused and pulsed laser radiation, triggering Ca^{2+} waves in the epidermis of live anesthetized mice with ubiquitous expression of a genetically encoded Ca^{2+} indicator. Waves expanded radially and rapidly, reaching up to eight orders of bystander cells that remained activated for tens of minutes, without displaying oscillations of the cytosolic free Ca^{2+} concentration ($[Ca^{2+}]_c$). By combining in vivo pharmacological dissection with mathematical modeling, we demonstrate that Ca^{2+} wave propagation depended primarily on the release of ATP, a prime damage-associated molecular patterns (DAMPs), from the hit cell. Increments of the $[Ca^{2+}]_c$ in bystander cells were chiefly due to Ca^{2+} release from the endoplasmic reticulum (ER), downstream of ATP binding to P2Y purinoceptors. ATP-dependent ATP release though connexin hemichannels (HCs) affected wave propagation at larger distances, where the extracellular ATP concentration was reduced by the combined effect of passive diffusion and hydrolysis due to the action of ectonucleotidases, whereas pannexin channels had no role. Bifurcation analysis suggests basal keratinocytes have too few P2Y receptors (P2YRs) and/or phospholipase C (PLC) to transduce elevated extracellular ATP levels into inositol trisphosphate (IP_3) production rates sufficiently large to sustain $[Ca^{2+}]_c$ oscillations.

Submitted: 25 July 2021; **Revised:** 23 November 2021; **Accepted:** 23 November 2021

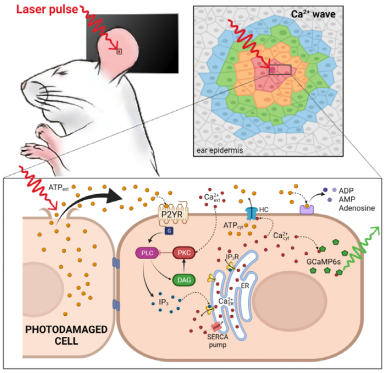

Key words: Skin; laser-induced intra-epidermal photodamage; wound healing; purinergic signaling; connexins; pannexins; reaction-diffusion equations; mathematical model

Introduction

The epidermis forms an essential barrier against dehydration and pathogens, as well as light, chemical and mechanical injury.[1,2] It is a stratified epithelium largely composed of keratinocytes (95%), melanocytes (that donate pigment to the keratinocytes), Langerhans' cells, which have immunological functions, and Merkel cells, also known as Merkel-Ranvier cells or tactile epithelial cells.[2] It is well established that epidermis' continuous renewal is sustained by stem cells contained in the *stratum basale*.[3–8] The differentiating keratinocytes are gradually displaced in the outward direction, from *stratum basale* through *stratum spinosum* to *stratum corneum*, where corneocytes are continually shed from the skin surface.[1,2] In different epithelia, including the epidermis, damage triggers perturbations of the $[Ca^{2+}]_c$ that spread from cell to cell, known as (intercellular) Ca^{2+} waves (see e.g. Refs.[9–14]) and considered a fundamental mechanism for coordinating multicellular responses.[15] Ca^{2+} signaling is at the core of epidermal homeostasis,[16–18] however, the mechanisms underlying Ca^{2+} wave propagation and their significance in the damaged epidermis are incompletely understood. A gradient of Ca^{2+} across the epidermis is key for keratinocyte differentiation and formation of the epidermal permeability barrier,[16–18] maintenance of which relies on a delicate balance between proliferation and differentiation, two Ca^{2+}-dependent cellular processes.[2,8,19] Defects of epidermal Ca^{2+} homeostasis cause skin pathologies, such as Darier's disease for which *ATP2A2* has been identified as the defective gene, indicating that the sarcoplasmic/endoplasmic reticulum Ca^{2+} ATPase (SERCA)2 plays a key role.[20]

ATP, which is present at mM concentration in the cytosol whereas its normal concentration in the extracellular environment is in low nM range, is released by most cells as an extracellular signaling molecule.[21,22] ATP release was detected in cultured human neonatal keratinocytes exposed to air,[23] as well as from injured mouse epidermal keratinocytes,[24] normal human epidermal keratinocytes (NHEKs) co-cultured with mouse dorsal root ganglion (DRG) neurons,[25] and HaCaT cells[26] (a spontaneously transformed aneuploid immortal keratinocyte cell line from adult human skin, with high capacity to differentiate and proliferate in vitro[27]). Extracellular ATP can affect the $[Ca^{2+}]_c$ by activating Ca^{2+}-permeable P2XRs[28] and/or by promoting Ca^{2+}-release from the endoplasmic reticulum (ER) via G-protein coupled P2YRs[29,30] on the surface of keratinocytes and other epidermal cells types.[31] Therefore, ATP release and purinergic signaling have the potential to interfere with epidermal homeostasis and have been implicated in a host of processes, including pain, inflammation and wound healing.[31]

In this study, we evoked Ca^{2+} waves by selectively photodamaging a single keratinocyte of the epidermal basal layer of the earlobe skin in live anesthetized mice. Our experimental model is related not only to accidental injury, but also to the medical practice of skin resurfacing/rejuvenation based on intra-epidermal focal laser-induced photodamage that is used to treat numerous conditions such as photodamage and acne scars, hidradenitis suppurativa and posttraumatic scarring from basal cell carcinoma excision.[32–35] As detailed in the following Methods and Results sections, we used intravital multiphoton microscopy to visualize Ca^{2+} waves in mice expressing GCaMP6s, a sensitive and selective genetically encoded Ca^{2+} indicator.[36] To dissect the molecular components contributing to Ca^{2+} wave propagation, we performed in vivo pharmacological interference experiments by intradermal microinjection of different drugs. With the insight gained from data analysis, we formulated a mathematical model that accounts for the observed Ca^{2+} dynamics based on ATP release and diffusion, and activation of P2YRs. The significance of our findings for wound healing and skin therapy is discussed in relation to Ca^{2+} signaling pathway activation in the epidermis.

Methods

Animals

Mice were bred and genotyped at the National Research Council-Institute of Biochemistry and Cell Biology (CNR-IBBC), Infrafrontier/ESFRI-European Mouse Mutant Archive (EMMA), Specific Pathogen-Free (SPF) barrier unit (Monterotondo Scalo, Rome). All the experimental procedures were agreed upon, reviewed and approved by local animals welfare oversight bodies and were performed with the approval and direct supervision of the CNR-IBBC/Infrafrontier—Animal Welfare and Ethical Review Body (AWERB), in accordance with general guidelines regarding animal experimentation, approved by the Italian Ministry of Health, in compliance with the Legislative Decree 26/2014 (ref. Project license 603/2018-PR), transposing the 2010/63/EU Directive on protection of animals used in research). In addition, all animal experimentation was conducted in adherence to the NIH Guide for the Care and Use of Laboratory Animals and recommendations from both ARRIVE and PREPARE guidelines.[37,38] Mice were housed in individually ventilated caging systems (Tecniplast, Gazzada, Italy) at a temperature (T) of 21

Table 1. Photodamage and image acquisition parameters

Parameter	Value
Excitation and photodamage wavelength	920 nm
Photodamage optical power in the focal plane	118 mW
Photodamage duration	500 ms
Average focal plane optical power used for imaging	25 mW
Frame size (pixels)	512 × 512
Pixel dwell time	81.2 ns
Raw frame rate	45.7 fps
Number of averaged frames	9
Effective frame rate	2.5 fps
Resolution	0.62 μm/pixel

± 2°C, relative humidity (RH) of 55 ± 15% with 50–70 air changes per hour (ACH) and under controlled (12 : 12 hour) light–dark cycles (7 am–7 pm). Mice had ad libitum access to water and a standard rodent diet (Emma 23, Mucedola, Settimo Milanese, Italy).

Adult transgenic mice, both male and female, aged between 5 and 40 weeks and ubiquitously expressing the Ca^{2+} biosensor GCaMP6s[36] were used for in vivo Ca^{2+} imaging experiments. These mice were generated in the animal facility of the laboratory by crossing the Jackson Laboratory strain #024106 (STOCK-Gt(ROSA)26Sor$^{tm96(CAG-GCaMP6s)Hze}$/J) with the European Mouse Mutant Archive (EM) Cre-deleter strain EM:01135 (B6.C-Tg(CMVcre) $^{1Cgn/CgnCnrm}$). Double mutant mice were identified amplifying tail genomic DNA by means of PCR. The presence of the CAG-GCamp6 insertion in the Rosa26 locus and the wild type allele were detected using the primers:

5'-ACG-AGT-CGG-ATC-TCC-CTT-TG-3', 5'- AAG-GGA-GCT-GCA-GTG-GAG-TA-3'

and

5'-CCG-AAA-ATC-TGT-GGG-AAG-TC-3'.

The CRE-deleter transgene was detected using the primer pair

5'-CGA-GTG-ATG-AGG-TTC-GCA-AG -3'

and

5'-TGA-GTG-AAC-GAA-CCT-GGT-CG -3'.

PCR products were run on 2% agarose gels, visualized with ethidium bromide and photographed. Expected band sizes were 450 bp for the CAG-GCamp6 and 297 bp for the wt allele and 390bp for the Cre transgene.

Multiphoton microscopy

System description

We used a custom-made multiphoton system (Figure S1) based on a Bergamo II architecture (Thorlabs Imaging System, Sterling, VI, USA), as previously described.[12] The system was equipped with two scanning heads, one with resonant-galvo (RG) mirrors and the other with galvo-galvo (GG) mirrors, and was coupled to a mode-locked titanium-sapphire (Ti:Sa) fs pulsed laser (Chameleon Vision II Laser, Coherent, Inc., Santa Clara, CA, USA) (Figure S2). The RG scanner was used for imaging, whereas the GG scanner was used to focally photodamage a pre-defined spot in the field of view (FOV) by focusing the collimated laser beam onto the sample through a 25× water- immersion objective (XLPLN25XWMP2, NA 1.05, Olympus Corporation, Tokyo, Japan; the same objective was also used for imaging).

Multiphoton excitation of GCamp6s was performed at 920 nm, whereas its emission signal was filtered by a single band-pass filter (Cat. No. FF02-525/40-25, Semrock/IDEX, Rochester, NY, USA) placed in front of a non-descanned GaAsP detector (Cat. No. H7422–50, Hamamatsu Photonics K.K., Shizuoka, Japan). Electro-optical modulators (EOM) and mechanical ultrafast shutters were used to control both photodamage and imaging light exposure using the ThorImage LS 3.1 software (Thorlabs). Parameters used for photodamage and image acquisition are listed in Table 1. Laser excitation intensity and frame averaging were adjusted to minimize photobleaching and phototoxicity, while achieving enough signal to noise ratio and temporal resolution.

Intravital multiphoton microscopy and drug delivery

Mice were anesthetized with an intraperitoneal (i.p.) injection of physiological solution containing 90 mg/kg ketamine and 0.5 mg/kg medetomidine. If the experiment duration was longer than 2 hours, half-dose of the anesthesia was reinjected to avoid mouse awaking. Mice were positioned on the stage of the multiphoton microscope equipped with a heated pad kept at 35°C for homeothermic control. Ca^{2+} signals were recorded from the basal keratinocytes of the mouse pinna (earlobe) skin, fixed under the objective with double-sided tape. For optical coupling, a drop of phosphate buffered saline (PBS) solution was placed between the skin and the 25× water-immersion objective lens. The PBS solution was composed of 10 mM Phosphate (as sodium phosphates), 2.68 mM KCl and 140 mM NaCl.

After positioning the animal under the microscope objective lens, we waited 10 minutes to allow intracellular Ca^{2+} (mobilized during earlobe manipulation) to return to baseline (as judged by low levels of GCaMP6s fluorescence). For each mouse, control photodamage experiments were repeated $n \geq 3$ times with similar results in different positions of the earlobe. Next, to block or enhance a specific pathway, the ear surface was gently cleaned and dried and a 4 μl solution containing a selected drug (Table 2) diluted in PBS was microinjected in the earlobe skin using a 10 μl NANOFIL syringe (World Precision Instruments Inc., Sarasota, FL, USA) equipped with a gauge 33 needle. The microinjected PBS solution also contained 1.78 μM of fluorescent Dextran Texas Red (molecular weight, MW = 70,000 Da; single-photon Excitation/Emission wavelengths = 595/615 nm; two-photon excitation wavelength = 920 nm) to confirm that the drug-containing fluid reached the imaged area. Thereafter, the same photodamage protocol used in the previous control recording was used to acquire image sequences in the presence of the

Table 2. Details of drugs used to dissect components of Ca^{2+} wave propagation mechanisms. The last column reports the serial number of the mice used for the corresponding experiments.

Reagent	Concentration	Part number	Supplier	Mouse #
Dextran Texas Red™	1.78 μM	D1830	ThemoFisher Scientific	1–18
Apyrase	500 U/ml	A2230	Merck & Co.	3, 4
PPADS	625 μM	P178	Merck & Co.	5, 6
ARL 67156	400 μM	A265	Merck & Co.	7, 8
EGTA	5 mM	E3889	Merck & Co.	9, 10
Thapsigargin	400 nM	T9033	Merck & Co.	11, 12
CBX	400 μM	C4790	Merck & Co.	13, 14
Probenecid	4 mM	P8761	Merck & Co.	15, 16
TAT-Gap19	200 μM	A230580	GenoSphere	17, 18

selected drug. A dedicated series of experiments was performed to verify that photodamage-evoked Ca^{2+} waves were insensitive to the presence of the microinjected fluorescent Dextran Texas Red. Due to its large MW, Dextran diffused slowly through the tight layers of keratinocytes and accumulated mainly in the extracellular spaces below the *stratum basale*. The investigator was not blinded during administration of treatments or result assessment. No samples were excluded from analyses. To minimize animal stress and avoid cross-interaction between different drugs, no more than one drug was injected in the same earlobe.

Images acquired with different PMTs of the multiphoton microscope are shown in Figure S3 together with the corresponding composite images. In general, a given focal plane intercepts furrows and bulges, exposing a multitude of cell populations and structures while performing intravital microscopy in the skin. Cells corresponding to different epidermal layers can be distinguished morphologically: smaller polygonal cells are keratinocytes of the *stratum basale*, while increasingly larger cells correspond to the suprabasal layers. Second-harmonic generation (SHG) images were acquired at 460/50 nm emission wavelength, allowing the imaging of collagen fibers (Figure S3 A, E). GCaMP6s fluorescence (and keratinocytes autofluorescence) contributed to the signal detected in the 525/40 nm emission channel (Figure S3 B, F). Images in Figure S3 C, G were acquired in the 647/70 nm emission channel respectively before and after the microinjection of fluorescent Dextran Texas Red.

Image processing and data analysis

To establish a relationship between the $[Ca^{2+}]_c$ and GCaMP6s fluorescence emission F, we treated GCaMP6s as a Ca^{2+} buffer (denoted as G) that is present in the cytosol at a concentration [G]. Chelation of Ca^{2+} by buffer G to form a complex CaG is described by the reaction:

$$[Ca^{2+}]_c + [G] \underset{k^G_{off}}{\overset{k^G_{on}}{\rightleftarrows}} [CaG]$$

and the corresponding kinetic equation:

$$\frac{d[CaG]}{dt} = k^G_{on}\ [Ca^{2+}]_c\,[G] - k^G_{off}\,[CaG]\,, \tag{E1}$$

where square brackets are used to indicate concentration, $k^G_{on} = 7.78\ \mu M^{-1}s^{-1}$ is the rate constant for Ca^{2+} binding to G and $k^G_{off} = 1.12\ s^{-1}$ is the rate constant for Ca^{2+} dissociation.[36]

At chemical equilibrium d [CaG]/dt = 0, therefore

$$\frac{[Ca^{2+}]_c[G]}{[CaG]} = \frac{k^G_{off}}{k^G_{on}} \equiv k^G_D, \tag{E2}$$

where k^G_D is the equilibrium or dissociation constant, thus

$$[Ca^{2+}]_c = k^G_D\ \frac{[CaG]}{[G]}. \tag{E3}$$

Assuming that [G] is low enough, *F* can be written as the following linear combination:

$$F = S_f\ [G] + S_b\,[CaG]\,, \tag{E4}$$

where the proportionality constant S_f and S_b lump all factors such as the illumination intensity, the efficiency of fluorescence emission, the molar absorption coefficient, and the length of the absorbing medium traversed by the illuminating beam. If c_T denotes the total (constant) fluorophore concentration, the mass balance equation is:

$$c_T = [G] + [CaG]\,. \tag{E5}$$

Defining the emission under Ca^{2+}-saturating and Ca^{2+}-free conditions respectively as $F_{max} = S_b\ c_T$ and $F_{min} = S_f\ c_T$, the expression for *F* can be re-written as

$$F = F_{min} + (S_b - S_f)\,[CaG] = F_{max} - (S_b - S_f)\,[G]\,, \tag{E6}$$

yielding

$$\frac{F - F_{min}}{F_{max} - F} = \frac{[CaG]}{[G]}\,. \tag{E7}$$

Combining equations E3 and E7, we conclude that

$$[Ca^{2+}]_c = k^G_D\ \frac{F - F_{min}}{F_{max} - F}. \tag{E8}$$

Equation E8 can be used to estimate the change in the $[Ca^{2+}]_c$,

$$\Delta[Ca^{2+}]_c \equiv [Ca^{2+}]_c - [Ca^{2+}]_0, \tag{E9}$$

where $[Ca^{2+}]_0$ is the pre-stimulus (baseline) concentration. For changes that fall within the approximately linear region of the input/output relation, we may write:

$$\Delta[Ca^{2+}]_c \cong \frac{d[Ca^{2+}]_c}{dF}(F - F_0) \cong k\frac{\Delta F}{F_0}, \quad \text{(E10)}$$

where F_0 is pre-stimulus fluorescence and

$$k \equiv k_D^G \frac{F_0(F_{max} - F_{min})}{(F_{max} - F_0)^2}. \quad \text{(E11)}$$

Thus, if imaging experiments are performed in such a way that photobleaching is negligible, and as long c_T and the optical path length do not change during the measurement, the pixel-by-pixel ratio

$$\frac{\Delta F}{F_0} \equiv \frac{F - F_0}{F_0} \quad \text{(E12)}$$

is a unique function of the stimulus-induced $\Delta[Ca^{2+}]_c$.[39]

On this ground, image processing and data analysis used to relate $\Delta[Ca^{2+}]_c$ and $\Delta F/F_0$ were carried out using the open source ImageJ software, the MATLAB programming environment (R2015a, The MathWorks, Inc., Natick, MA, USA) and Vimmaging, a custom-made software developed under the MATLAB environment by Catalin D. Ciubotaru and Fabio Mammano. To automatically select cell boundaries in an image obtained by averaging all frames in a calcium wave, we used *roiSelection*, a Matlab graphics user interface (GUI) developed by Catalin D. Ciubotaru.

To eliminate contributions independent of GCaMP6s expression, all image analyses were preceded by background subtraction. To define the background-subtraction procedure, four images of basal layer keratinocytes were recorded from a wild type mouse (not expressing GCaMP6s, Figure S4) under the same conditions used for all other experiments (see Table 1). Histograms of pixel intensity x were extracted from regions of interest (ROIs) of 76×76 pixels with ImageJ and fitted with a Gaussian distribution

$$G_1 = A_1 \cdot exp\left[\frac{-(x - \mu_1)^2}{2\sigma_1^2}\right]. \quad \text{(E13)}$$

The fitting parameters for wild type mouse epidermis were $\mu_1 = 440 \pm 1$ and $\sigma_1 = 31 \pm 4$.

Next, we examined basal layer keratinocytes in a cohort of $n = 15$ GCaMP6s-expressing mice. The distribution of baseline pixel intensity values in ROIs composed of 76×76 pixels, averaged over the first 5 frames preceding the photodamage stimulus (that occurred at frame 6), followed a bimodal distribution that was well fitted by the sum of two Gaussians, $G_1 + G_2$, where

$$G_2 = A_2 \cdot exp\left[\frac{-(x - \mu_2)^2}{2\sigma_2^2}\right]. \quad \text{(E14)}$$

The parameters $\mu_1 = 440 \pm 2$ and $\sigma_1 = 30 \pm 1$ (mean ± s.e.m.) of G_1 for the GCaMP6s samples were not significantly different from those of the wild type control ($p = 0.98$ for μ_1; $p = 0.5$ for σ_1; t-test). In contrast, the parameters $\mu_2 = 697 \pm 9$ and $\sigma_2 = 206 \pm 5$ (mean ± s.e.m.) of G_2 differed significantly from those of the wild type control ($P = 2\times10^{-10}$ for μ_1; $P = 2\times10^{-12}$ for σ_1; t-test). Therefore, we attributed the pixel intensity distributions corresponding to G_1 to the sum of instrument noise/offset plus keratinocyte autofluorescence, and the distributions corresponding to G_2 to GCaMP6s pre-stimulus (baseline) fluorescence. Based on this analysis, the intersection between the two fitting curves (Figure S5, vertical dash-dotted lines), was selected as the threshold value to be subtracted from each image of the corresponding sequence. All pixel values below threshold were set to 1, thus eliminating autofluorescence and the instrumental offset. Thereafter, Ca^{2+} signals evoked by photodamage were quantified as the time-dependent background-subtracted pixel-by-pixel relative changes in fluorescence, $\Delta F(t)/F_0$, where F_0 is the pre-stimulus fluorescence obtained by averaging over the first 5 (pre-stimulus) frames.

Statistical analysis

Mean values are quoted ± standard error of the mean (s.e.m.). Comparisons of means for non-Gaussian sample distributions were made using the Wilcoxon Rank sum test (as implemented in the Matlab function *ranksum*). For samples that had Gaussian distribution, the two-sample t-test (as implemented in the Matlab function *ttest2*) was adopted; $P = P\text{-value} < 0.05$ was assumed as statistically significant.

Immunofluorescence

Adult mice were euthanized by cervical dislocation. Hair was gently removed from earlobe skin by applying hair removal cream for 3 min. Thereafter the cream was removed with cotton buds and the skin surface was rinsed with PBS. Earlobes were then excised and immersed in PBS.

For whole mount preparations, skin (dermis and epidermis) was mechanically detached from the underlining cartilage and transferred in a Petri dish containing ice-cold PBS. Dermal fat was gently peeled off with a scalpel. The skin sample was then divided in about 3 × 3 mm^2 portions, immersed in ice-cold PFA (4%) and shaken gently for 1 hour at 4°C.

For slice preparations, ~1 mm-thick slices were obtained from the earlobe sample by free-hand cutting with a scalpel. Slices were then immersed in ice-cold PFA (4%) and shaken gently for 1 hour at 4°C.

After fixation as described above, whole mount and slice preparations were washed 3 times for 5 min in 1 mL of PBS and incubated for 30 min at room temperature in blocking buffer [PBS complemented with 10% heat-inactivated fetal bovine serum (FBS, 10% v/v, Cat. No. 10270-106, Thermo Fisher Scientific) and 0.2% Tryton X-100 (TX-100, #X100, Sigma)]. Samples were then incubated overnight in a humidified chamber at 4°C with primary anti-$P2Y_1R$ or anti-$P2Y_2R$ antibodies (#APR-009 and #APR-010, respectively, Polyclonal, knock out-validated, Alomone Labs, Jerusalem, Israel) diluted 1:100 in blocking buffer. The next day, samples were washed 3 times for 15 min at room temperature with washing buffer (2% FBS diluted in PBS with 0.2% TX-100) and incubated with cross-adsorbed Alexa Fluor 488 secondary antibody (1:500, #A-11008, Thermo Fisher Scientific) for 1 h at room temperature. Then, samples were washed 3 times for 15 minutes in washing buffer at room temperature and stained with DAPI (5 μM in washing buffer for 5 min). Samples were finally mounted in a liquid anti-fade medium (Mowiol 4–88) between a microscope slide and a coverslip. After 2 hours, coverslips were sealed with nail polish.

Fluorescence images acquisition was performed with a confocal TCS SP5 microscope (Leica) equipped with a 63× oil immersion objective (HC PL Apo, UV optimized, NA 1.4, Leica). DAPI, Alexa 488 and autofluorescence signal were excited with 405 nm, with 488 nm and with 543 nm laser light, respectively. DAPI fluorescence was collected between 415 nm and 480 nm; Alexa Fluor 488 fluorescence was collected between 500 nm and 540 nm; skin autofluorescence was collected between 625 nm and 700 nm. Images were acquired by averaging each line 32 times in a line-by-line sequential protocol (total pixel dwell time about 2.5 ms; pixel size, 120 nm).

Mathematical model

The model we developed is based on radial ATP diffusion from the damaged cell, signaling via P2YRs, PLC and IP_3Rs, and the following geometrical arrangement. The photodamaged cell was modeled as a cylinder with radius 5 μm, height 10 μm and center at $r = 0$ μm. The upper surface of the cell hit by laser radiation was assumed to burst open at time $t = 0$ seconds, so that its cytosolic ATP content diffused first in the space just above the cell, then radially in the thin (20 nm) clefts between the tightly packed sheets of epidermal keratinocytes.[40] We assumed 2-dimensional radial symmetry and discretized the inter-sheet space into 20 rings of radial length $a = 10$ μm, corresponding to the cellular diameter. ATP in each ring stimulated IP_3 production (via P2YRs and PLC) in the adjacent cells above and below the ring, and – vice versa – these cells were allowed to release ATP via connexin HCs into the inter-sheet clefts. The equations for ATP dynamics are[41]

$$\begin{aligned}\frac{dA_c}{dt} &= -\frac{D}{ah}(A_c - A_0),\\ \frac{dA_0}{dt} &= \frac{D}{h^2}(A_c - A_0) + \frac{4D}{d^2}(A_1 - A_0) - kA_0,\\ \frac{dA_j}{dt} &= \frac{D}{2ja^2}((2j+1)A_{j+1} - 4jA_j + (2j-1)A_{j-1}) - kA_j + J_{HC,j},\end{aligned} \tag{M1}$$

where A_c is the ATP concentration in the photodamaged cell, A_0 is the ATP concentration in the disk above the damaged cell, and A_j is the ATP level in ring number j of the inter-sheet space, D is the effective diffusion constant of ATP, $h = 0.02$ μm is the height of the space between cellular sheets,[40] k is the degradation rate of ATP, and $J_{HC,j}$ is the flux of ATP via HCs, which is assumed to be a steep Hill-function of the intracellular calcium concentration (Ca) in cell j,[42]

$$J_{HC,j} = \frac{V_{HC}\, Ca_j^8}{Ca_j^8 + (0.3\ \mu\mathrm{M})^8}. \tag{M2}$$

ATP binding to P2YRs activates PLC, which produces IP_3 from PIP_2. All isoforms of PLC depend on Ca^{2+},[43] and in particular PLC-δ, which is expressed in keratinocytes[44] and is activated by intracellular Ca^{2+}.[45–47] We therefore introduced a feedback term ψ from Ca^{2+} onto the rate of IP_3 production. IP_3 dynamics in cell j was described by the equations

$$\frac{dIP_{3,j}}{dt} = (1+\psi_j)\frac{V_{PLC}\, A_j}{A_j + K_{PLC}} - k_{IP3}IP_{3,j}, \tag{M3}$$

$$\frac{d\psi_j}{dt} = \frac{\psi_\infty(Ca_j) - \psi_j}{\tau_\psi}, \tag{M4}$$

where $\psi_\infty(Ca) = \frac{\psi_{max}\, Ca}{Ca + (0.3\ \mu\mathrm{M})}$ and $\tau_\psi = 30$ s.

Finally, we modelled cytosolic Ca^{2+} dynamics by treating the cell cytoplasm as a *well stirred* closed compartment. Hence, the equation for cytosolic free Ca^{2+} in cell j reads

$$\frac{dCa_j}{dt} = J_{IP3R} + J_{leak} - J_{SERCA} - J_{buff}, \tag{M5}$$

where J_{IP3R} is IP_3-dependent Ca^{2+} flux from the ER to cytosol through IP_3Rs, which we modelled in accord with the Li-Rinzel model[48] (see below),

$$J_{leak} = L(Ca_{ER,j} - Ca_j) \tag{M6}$$

represents IP_3-independent Ca^{2+} flux from the ER to cytosol, and

$$J_{SERCA} = \frac{V_{SERCA}Ca_j^2}{Ca_j^2 + (0.2\ \mu\mathrm{M})^2} \tag{M7}$$

represents pumping from the cytosol to the ER by sarco/endoplasmic reticulum Ca^{2+}-ATPases (SERCA pumps).

The free Ca^{2+} concentration in the ER is linked to the Ca_j by the conservation equation

$$\alpha C\, a_{ER,j} = Ca_{TOT} - Ca_j, \tag{M8}$$

where α denotes the ratio of ER to cytosol volume and Ca_{TOT} stands for total Ca^{2+} present within the j-th cell (part in the cytosol, part in the ER). Further, J_{buff} is used to model Ca^{2+} buffering, where, for simplicity, endogenous buffers are assumed to have total concentration twice the concentration of GCaMP6 and to have the same kinetics as GCaMP6. These assumptions lead to

$$J_{buff} = 3J_{GCaMP6} = 3(k_{on}^G(G_T - CaG_j)Ca_j - k_{off}^G CaG_j). \tag{M9}$$

The Li-Rinzel model for IP_3 receptors[48] assumes that Ca^{2+} and IP_3 rapidly and independently activate the channels, whereas Ca^{2+} more slowly inactivates the channels. The Ca^{2+} flux from ER to cytosol through the IP_3Rs in cell j was modeled as

$$J_{IP3R} = k_{IP3R}\left(\frac{IP_{3,j}}{IP_{3,j} + K_i}\right)^3\left(\frac{Ca_j}{Ca_j + K_a}\right)^3 h_j^3(Ca_{ER,j} - Ca_j), \tag{M10}$$

where the inactivation variable h follows Hodgkin-Huxley-like dynamics,

$$\frac{dh_j}{dt} = A[K_d - (Ca_j + K_d)h]. \tag{M11}$$

To relate model and experimental GCaMP6 signals, we used the following equation representing binding/unbinding of cytosolic Ca^{2+} to GCaMP6s,

$$\frac{dCaG_j}{dt} = J_{GCaMP6} = k_{on}^G(G_T - CaG_j)Ca_j - k_{off}^G CaG_j, \tag{M12}$$

normalized the simulated CaG traces within the interval [0,1] and compared them to the corresponding normalized experimental traces.

The differential equations listed above were solved by using the stiff ode15s solver in MATLAB™ version 2019a (The MathWorks Inc., Natick, MA, USA). Model parameters in Table 3 were chosen to give reasonable fits, both quantitatively and qualitatively, to a series of experiments.

Results

Dynamics of Ca^{2+} waves elicited by focal intradermal photodamage in the earlobe skin of live anesthetized mice

To photodamage a single keratinocyte in the basal epidermal layer of earlobe skin in live anesthetized mice expressing the

Table 3. List of model parameters

Parameter	Unit	Value	Description
D	$\mu m^2/s$	65	Effective ATP diffusion constant
k	s^{-1}	0.27	ATP degradation constant
a	μm	10	Cell diameter (and radial discretization step size)
h	μm	0.02	Height of space between adjacent cellular sheets
V_{HC}	$\mu M/s$	1200	Maximal ATP release rate though connexin HCs
V_{PLC}	$\mu M/s$	1.85	Maximal rate of PLC production
K_{PLC}	μM	1.05	ATP EC_{50} value for PLC production
k_{IP3}	s^{-1}	15	IP_3 degradation rate
ψ_{max}	-	0.6	Maximal feedback strength from Ca^{2+} onto PLC
τ_ψ	s	30	Time-constant of feedback from Ca^{2+} onto PLC
L	s^{-1}	0.5	Leak rate
V_{SERCA}	$\mu M/s$	65	Maximal SERCA pump rate
α	-	0.1	Ratio between cytosolic and ER volumes
Ca_{TOT}	μM	2	Total amount of free cellular Ca^{2+}
k_{IP3R}	$\mu M/s$	42625	Maximal IP_3R release rate
K_i	μM	1	Li-Rinzel model parameter for IP_3 receptor activation by IP_3
K_a	μM	0.4	Li-Rinzel model parameter for IP_3 receptor activation by Ca^{2+}
K_d	μM	0.4	Li-Rinzel model parameter for IP_3 receptor inactivation by Ca^{2+}
A	$\mu M^{-1}\ s^{-1}$	5	Li-Rinzel model parameter for IP_3 receptor inactivation by Ca^{2+}
k_{on}^G	$\mu M^{-1}\ s^{-1}$	7.78	Ca^{2+}-GCaMP6s association constant[129]
k_{off}^G	s^{-1}	1.12	Ca^{2+}-CaGCaMP6s dissociation constant[129]
G_T	μM	7.4	Total GCaMP6s concentration[130]

GCaMP6s Ca^{2+} indicator, we used the second scanning head of the multiphoton microscope (GG branch of the optical path, see Methods). Ca^{2+} waves propagated radially from the damaged to the surrounding/bystander epidermal cells (referred to as expansion phase, Figure 1 A). Fluorescence signals persisted for several minutes in keratinocytes invaded by the Ca^{2+} wave, and slowly returned to basal levels (referred to as waning phase, Figure 1 B). Mean ± s.e.m. of the area $A(t)$ invaded by the Ca^{2+} wave are shown for both expansion and waning phases in Figure 1 C, D. $A(t)$ was computed by counting all pixels in which $\Delta F\ (t)/F_0$ (see Methods) exceeded an arbitrary threshold, corresponding to 30% of the maximum signal achieved as a result of photodamage in the given image sequence.

The volume of tissue invaded by the Ca^{2+} wave at the time of maximal expansion ($V = 1.2 \pm 0.2 \times 10^5\ \mu m^3$) was visualized by acquiring through-focus image sequences (also known as z-stacks) at 2 μm increments along the optical axis (z) of the objective lens (Figure 1 E, F). The graph $A(z)$ of the invaded area vs. depth (Figure 1 G) shows that Ca^{2+} waves extended up to ~10 μm above the photodamage plane, and occasionally stimulated cells with the typical morphology of Langerhans cells, reaching the surface of the thin earlobe mouse skin (corneocyte layer). In the opposite, dermal direction, Ca^{2+} waves reached down to ~20 μm below the photodamage plane invading the fibroblast-populated collagen matrix. Given the approximate radial symmetry of Ca^{2+} waves during the expansion phase in the focal plane, the equivalent radius of the invaded area was computed as

$$R\ (t)\ = \sqrt{A(t)\ /\pi} \tag{R1}$$

(Figure 2 A). The maximal value $R_{max} = \max[R\ (t)]$ averaged over the control experiments that gave the largest waves was 67 ± 1 μm (mean ± s.e.m.; $n = 21$ experiments in 6 mice).

To further characterize the expansion phase, we computed whole-cell $\Delta F\ (t)/F_0$ responses by spatially averaging pixel signals over individual bystander keratinocytes. Data from different keratinocytes in different experiments were grouped and averaged based on the distance d of the cell centroid from the photodamage site in the range from 10 ± 3 μm to 80 ± 3 μm (Figure 3 A). Note that this range exceeds the average value of R_{max} given above. The discrepancy is due to the 30% threshold criterion used to select pixels that contributed to the estimate of the area $A(t)$ invaded by the Ca^{2+} wave. In general $\Delta F\ (t)/F_0$ responses at 70 ± 3 μm and 80 ± 3 μm remained subthreshold, and therefore did not contribute to $A(t)$.

From the analysis of $\Delta F\ (t)/F_0$ traces, we extracted 3 parameters for each order of bystander keratinocytes. The first parameter is the amplitude reached at time $t = 20$ s,

$$a_{20s} \equiv \left.\frac{\Delta F}{F_0}\right|_{t=20s}, \tag{R2}$$

which decreased slowly with d, up to a critical value d_{stop} (typically comprised between 70 μm and 80 μm) beyond which wave propagation ceased abruptly and a_{20s} approached zero (Figure 3 B).

The second parameter is the Ca^{2+} load imparted on the cell by the Ca^{2+} wave, computed as the integral

$$I \equiv \int_{t_1}^{t_2} \frac{\Delta F\ (t)}{F_0} dt, \tag{R3}$$

where $t_1 = 0$ and $t_2 = 20$ s. I increases if the amplitude of $\Delta F\ (t)/F_0$ increases and/or the velocity of wave propagation increases (due to the fixed limits of the integration interval). For the same reason, due to the progressively delayed rise of the Ca^{2+} response, I decreases with d (Figure 3 C).

The third parameter is the response speed of the cell

$$s \equiv \max\left[\frac{d}{dt}\left(\frac{\Delta F\ (t)}{F_0}\right)\right], \tag{R4}$$

computed as the slope of the trace around the inflection point of its rising phase. Clearly, s depends both on the velocity of wave propagation and the kinetics of the signal transduction chain that promotes the $[Ca^{2+}]_c$ increase in the given cell. Altogether,

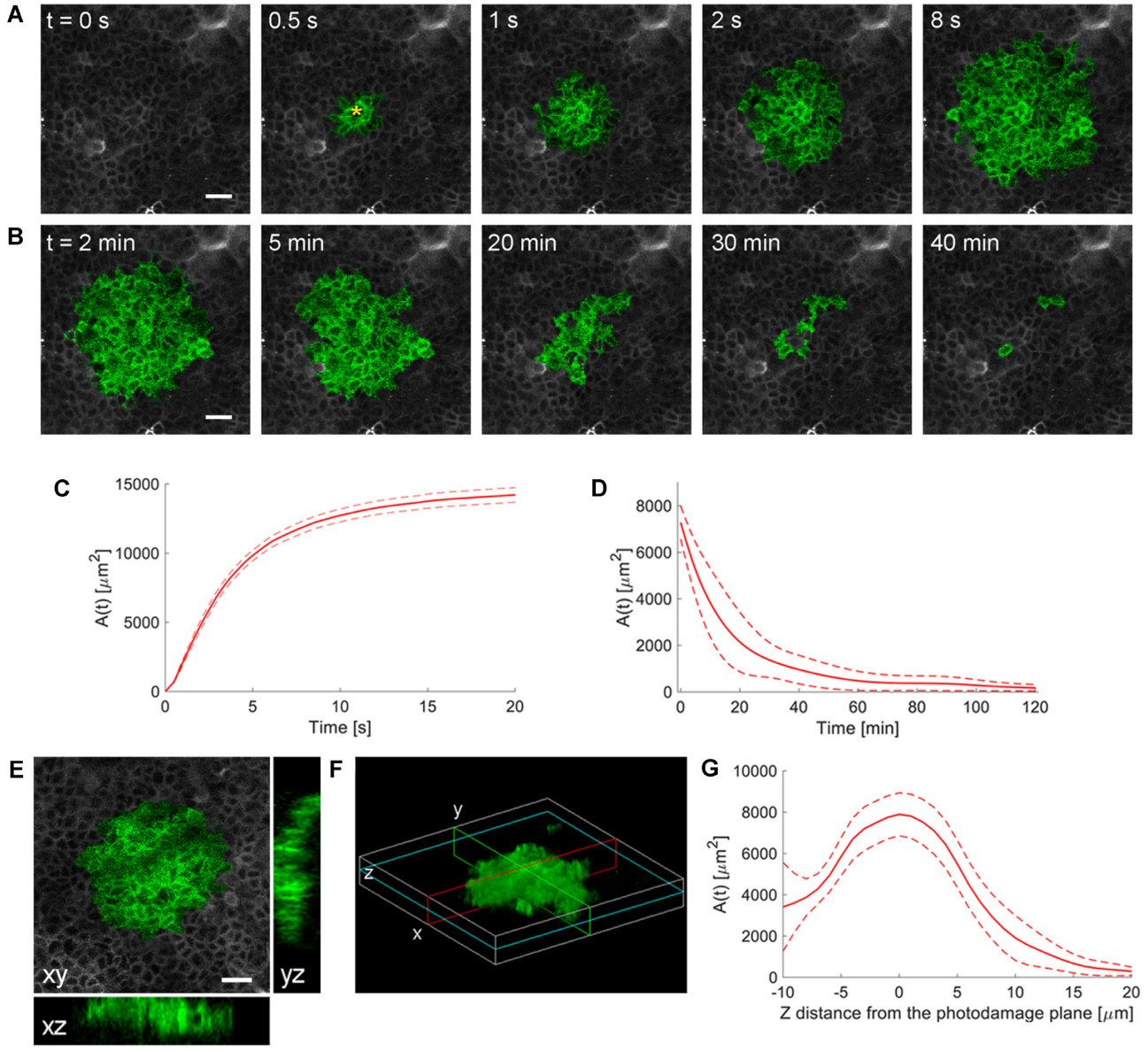

Figure 1. Intravital multiphoton microscopy of Ca^{2+} waves elicited by focal photodamage in the epidermal basal layer of earlobe skin in live anesthetized mice. (**A, B**) Representative sequences of GCaMP6s fluorescence images acquired at shown time points from the instant preceding the beginning of the photodamage (t = 0 s) showing (**A**) Ca^{2+} wave expansion from the photodamage site (yellow asterisk in the 0.5 s image) and (**B**) subsequent wave waning. (**C, D**) Invaded area vs. time, A(t), during Ca^{2+} wave expansion (**C**) and waning (**D**). (**C**) Mean (solid line) ± s.e.m. (dashed lines) of $n = 60$ experiments in 14 mice. (**D**) mean (solid line) ± s.e.m. (dashed lines) of $n = 3$ experiments in 1 mouse. (**E, F**) Volume of tissue invaded by the Ca^{2+} wave after focal photodamage. (**E**) Views of the wave in the xy plane (focal plane) and two orthogonal (xz and yz) planes. (**F**) 3D rendering of the volume invaded by the wave; cyan, red and green lines indicate the xy, xz and yz planes of panel (**E**), respectively. (**G**) Invaded area vs. axial coordinate (z, along the optical axis of the objective lens); data are mean (solid line) ± s.e.m. (dashed lines) of n = 7 experiments in 1 mouse. Scale bars in **A**, **B**, **E**: 25 μm.

a cohort of 17 control mice were used to generate the data presented in Figures 1-3. The results show that *s* was a monotonically decreasing function of *d* (Figure 3 D).

To explore the mechanisms underlying the propagation of Ca^{2+} waves, we used different drugs (Table 2) that interfere (more or less specifically) with candidate pathways. A different cohort of 18 mice were used for these *in vivo* pharmacological interference experiments, whose results are summarized graphically in Figure 4 and described in detail hereafter and in the Figures S6-S14.

Initially, a dedicated set of experiments were conducted to ascertain the effects of microinjecting solely vehicle solution (VS = PBS supplemented with Dextran Texas Red, 1.78 μM; see Methods) in the earlobe skin proximal to the photodamage site. Statistical analyses of the results indicate that the parameters used to characterize wave expansion after photodamage were largely unaffected by VS microinjection (Figure S6). Because VS injection had no significant influence on the parameters used to characterize quantitatively the expansion phase of Ca^{2+} waves, all successive experiments were performed in the following way: (1) a certain number of waves (used as reference) were evoked in $n \geq 3$ non-overlapping areas of the naïve mouse earlobe epidermis; thereafter, (2) different areas of the same earlobe were microinjected with the drug of interest dissolved in VS and a (3)

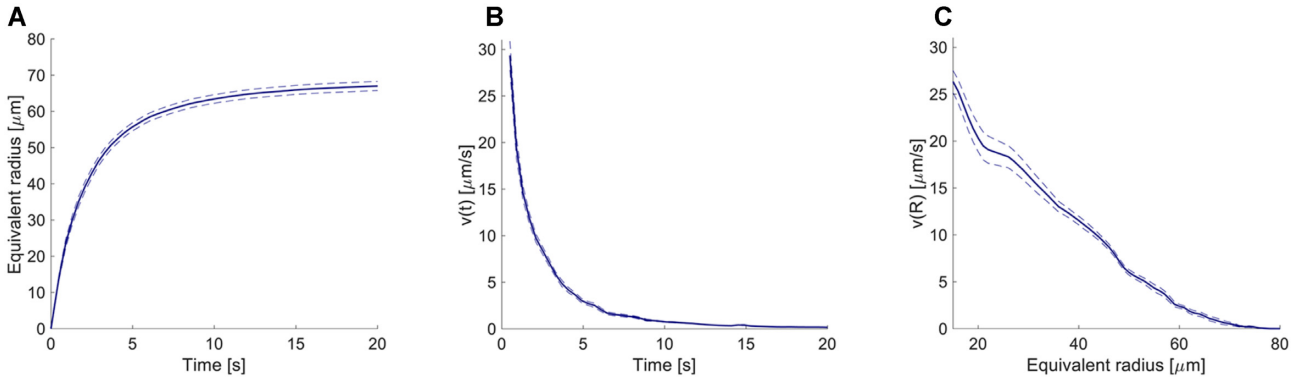

Figure 2. Detailed analysis of the expansion phase. (**A**) Equivalent radius of the area invaded during Ca^{2+} wave expansion. (**B**) Propagation velocity of the Ca^{2+} wave as function of time and (**C**) of the equivalent radius. Mean (blue solid lines) ± s.e.m. (blue dashed lines) of $n = 21$ experiments in 6 mice.

second set of waves were evoked (in $n \geq 3$ non-overlapping areas reached by Dextran Texas Red), (4) recorded and (5) compared with the previously acquired reference waves.

Based on co-injected Dextran Texas Red fluorescence, microinjected drugs diffused in an area with a diameter of about 3 mm, wide enough to contain more than 20 non-overlapping fields of view (FOVs). In each non-overlapping FOV, a single photodamage experiment was carried out generating a wave that remained completely confined within the FOV (Figure S15).

Critical role of ATP release in photodamage-induced Ca^{2+} waves

ATP in the extracellular milieu may couple to P2 purinoceptors on the cell plasma membrane to develop Ca^{2+} waves with or without involvement of IP_3 diffusion through intercellular gap junction channels (IGJCs).[15] To test the hypothesis that photodamage triggered Ca^{2+} waves by promoting ATP release from the photodamaged keratinocyte, we injected 4 μl of VS containing apyrase (500 U/mL), an enzyme that catalyzes ATP hydrolysis.[49] The presence of microinjected apyrase in the extracellular milieu correlated with a highly significant reduction of the invaded area A (t), therefore also of the equivalent Ca^{2+} wave radius R (t) (Figure S7 A, A'). From the same experiments, we derived and analyzed $\Delta F(t)/F_0$ traces from bystander keratinocytes and confirmed that apyrase severely hampered Ca^{2+} wave propagation, such that keratinocytes at distances $d > 20$ μm from the photodamage site failed to respond (Figure S7 D, D'). Consequently, all three critical parameters used to characterize these responses (a_{20s}, I and s) were null at $d > 20$ μm (Figure 4A, Figure S7 E-G, E'-G').

To determine whether P2 purinoceptors contributed to photodamage-evoked Ca^{2+} waves, we verified P2YR expression in keratinocytes of basal layer of the earlobe epidermis by immunofluorescence analysis with specific knock-out validated antibodies against $P2Y_1R$ and $P2Y_2R$ (Figure S16). Next, we microinjected 4 μl of VS containing pyridoxal phosphate-6-azo (benzene-2,4-disulfonic acid) tetrasodium salt hydrate (PPADS, 625 μM), a P2 purinoceptor antagonist.[31,50] PPADS reduced significantly the area invaded by Ca^{2+} waves following focal photodamage (Figure S8 A, A') and slowed down significantly $\Delta F(t)/F_0$ responses in all bystander keratinocytes (Figure S8 B-D, B'-D'). The parameters a_{20s}, I and s were significantly reduced in PPADS compared to controls at $d > 30$ μm, and the arrest distance d_{stop} decreased from 80 μm (control) to 50 μm (PPADS) (Figure 4 B, Figure S8 E-G, E'-G').

Once released in the extracellular space, ATP is rapidly hydrolyzed by cell surface-located ectonucleotidases, in particular by members of the ecto-nucleoside triphosphate diphosphohydrolase family (NTPDase1,2,3, and 8).[51–53] Therefore, we predicted that interfering with ectonucleotidase function should influence Ca^{2+} wave propagation. To test this hypothesis, we injected 4 μl of VS containing ARL 67156 trisodium salt hydrate (shortened as ARL, 400 μM), a widely used NTPDase inhibitor.[54–56] The presence of microinject ARL in the extracellular milieu correlated with a significant increase of the area $A(t)$ invaded by Ca^{2+} waves, hence of $R(t)$ (Figure S9 A, A'). ARL increased also the velocity $v(t)$ of Ca^{2+} wave propagation (Figure S9 B, C, B', C'), confirmed by the significantly reduced lag with which $\Delta F(t)/F_0$ traces grew after photodamage in bystander keratinocytes at $d > 20$ μm (Figure S9 D, D'). In addition, ARL increased significantly the parameters a_{20s}, I and s at $d > 40$ μm (Figure 4C, Figure S9 E-G, E'-G').

Together, the results in Figures S7-S9 indicate that (ii) extracellular ATP is a key signaling molecule underlying Ca^{2+} wave propagation in the photodamaged epidermis; (ii) the area A (t) invaded by the Ca^{2+} wave and its velocity of propagation v (t) depend on degradation of extracellular ATP by NTPDases expressed by epidermal keratinocytes (which can be partially inhibited by ARL).

Role of extracellular Ca^{2+}

To determine the role of extracellular Ca^{2+} in the dynamics of photodamage-evoked Ca^{2+} waves, we microinjected 4 μl of VS containing 5 mM EGTA, a widely used Ca^{2+} chelator.[57] Reduction of the extracellular free Ca^{2+} concentration ($[Ca^{2+}]_{ex}$) with EGTA caused a paradoxical enhancement of the invaded area, gauged by the effective radius R (t) (Figure S10 A, A'), paralleled by a significant increase of $\Delta F(t)/F_0$ bystander responses at all distances within 60 μm from the photodamaged cell (Figure S10 D, D'). The parameters a_{20s}, I and s were significantly increased in EGTA compared to controls, and the arrest distance d_{stop} increased from 70 μm (control) to 80 μm (EGTA) (Figure 4D, Figure S10 E-G, E'-G').

Because EGTA increased Ca^{2+} responses, Ca^{2+} influx through plasma membrane channels (including P2XRs[28]) did not to contribute significantly to the observed increments of the $[Ca^{2+}]_c$. Hence, the latter should be attributed chiefly to signal transduction through P2YRs, via the coupling to G proteins, activation of PLC, leading to the formation of IP_3 and release of Ca^{2+} from intracellular stores.[29–31,58]

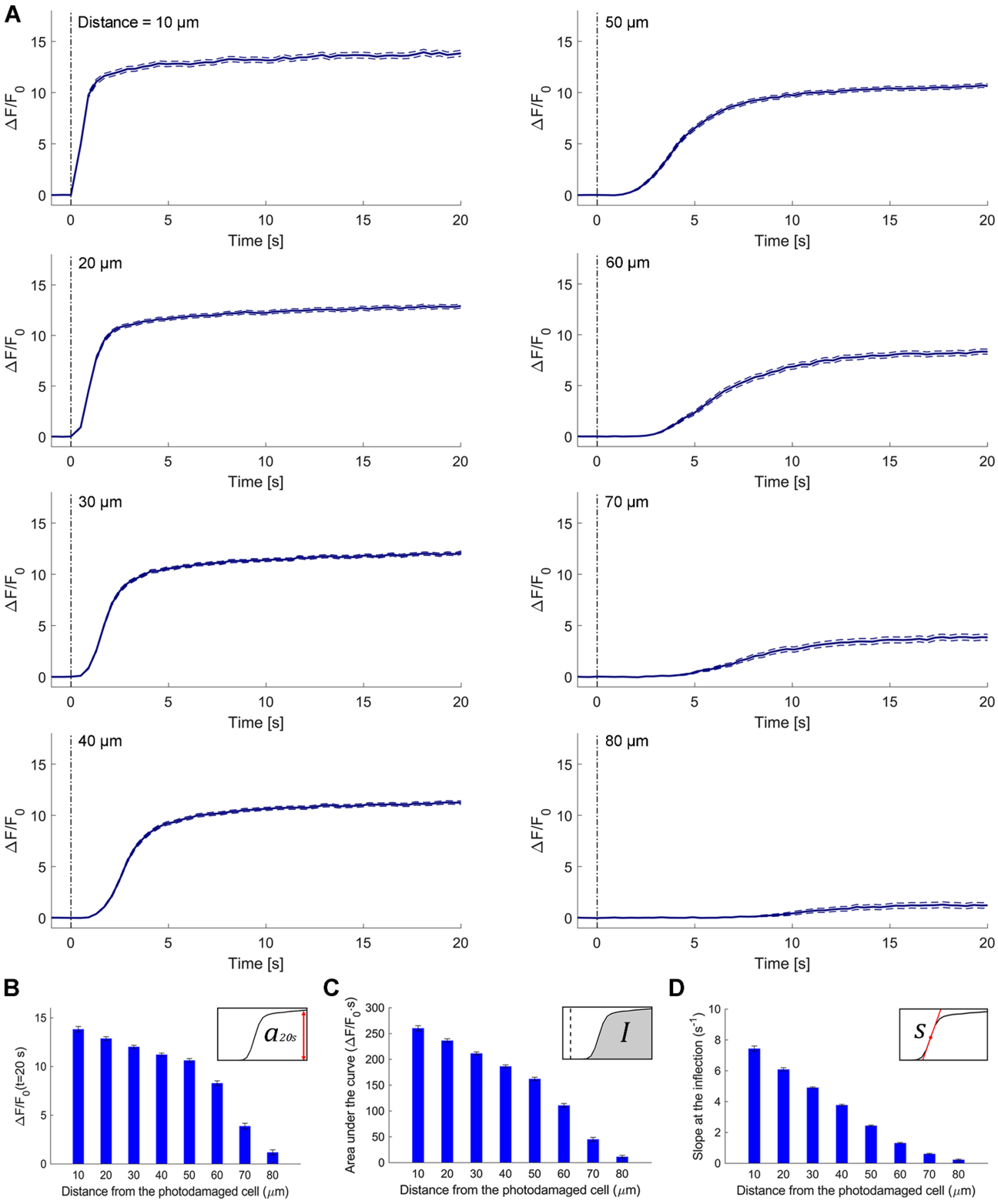

Figure 3. Analysis of GCaMP6s fluorescence changes in bystander keratinocytes at increasing distance from the photodamage site. (**A**) In each panel, the vertical black dash-dotted line at 0 s marks the end of the 0.5 s photodamage time interval. Data are mean (solid line) ± s.e.m. (dashed lines) vs. time for n = 60 experiments in 15 mice. (**B**) Amplitude (a_{20s}) of the $\Delta F(t)/F_0$ signal at time t = 20 s. (**C**) Area (I) under the $\Delta F(t)/F_0$ trace, computed between 0 and 20 s. (**D**) Slope (s) of the $\Delta F(t)/F_0$ trace at the inflection point (mean ± s.e.m). Data in (**B-D**) are mean ± s.e.m. vs. bystander cell distance from the photodamage site.

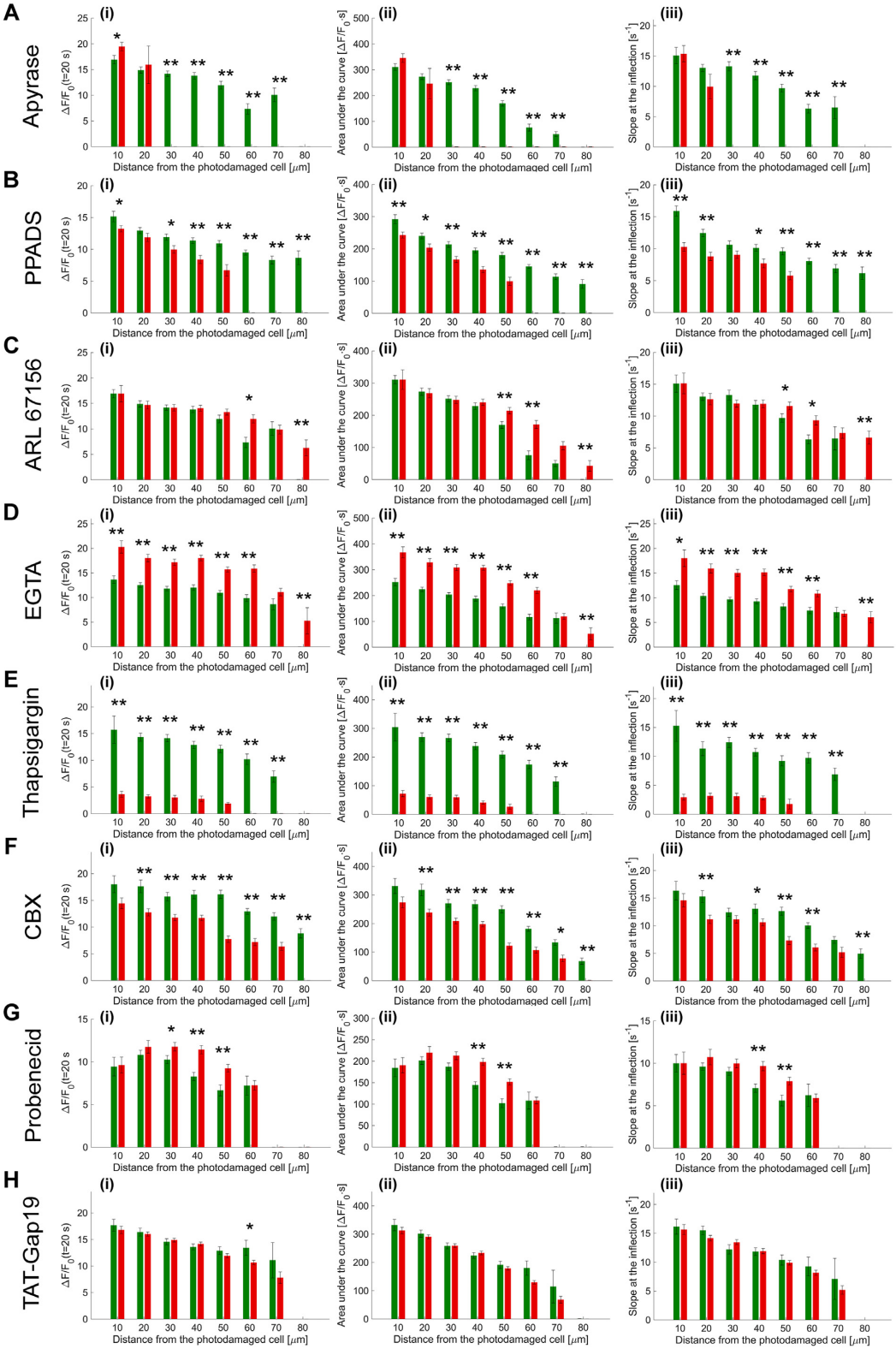

Figure 4. Summary of pharmacological interference experiments results. **(i)** Amplitude (a_{20s}) of the $\Delta F(t)/F_0$ signal at time t = 20 s. **(ii)** Area (I) under the $\Delta F(t)/F_0$ trace, computed between 0 and 20 s. **(iii)** Slope (s) of the $\Delta F(t)/F_0$ trace at the inflection point (mean ± s.e.m). Data are mean ± s.e.m. vs. bystander cell distance from the photodamage site in control conditions (green) and after VS microinjection (red) containing one of the following drugs: apyrase 500 U/ml (**A**), PPADS 625 μM (**B**), ARL 400 μM (**C**), EGTA 5 mM (**D**), thapsigargin 400 nM (**E**), carbenoxolone 200 μM (CBX, **F**), probenecid 4 mM (**G**), TAT-Gap19 200 μM (**H**). Significant differences are shown above each pair of bars (two-sample t-test): $* = P$-value < 0.05; $** = P$-value < 0.005.

Role of Ca^{2+} release from the ER

To corroborate the involvement of Ca^{2+} release from the ER downstream of P2YRs activation by extracellular ATP, we microinjected 4 μl of VS containing 400 nM of thapsigargin (previously dissolved in DMSO), a potent, cell-permeable, selective and irreversible inhibitor of the sarcoplasmic and endoplasmic reticulum Ca^{2+}-ATPase family (SERCA pumps).[59] As expected, thapsigargin caused a significant increase in the basal level of GCaMP6s fluorescence, F_0, from 190 ± 20 gray levels (GLs) in control conditions to 335 ± 5 GLs in thapsigargin ($P = 0.01$, two-sample t-test) due to uncompensated passive leakage of Ca^{2+} from the ER. Thapsigargin caused Ca^{2+} waves to propagate over smaller distances, significantly reducing the equivalent radius R (t) of the invaded area (Figure S11 A, A'). Moreover, the increased F_0 values caused an evident reduction of $\Delta F(t)/F_0$ bystander responses at any order of distance and consequent significantly reduced a_{20s} (Figure S11 D, D', Figure 4 E(i), Figure S11 E, E'). Also the parameters I and s were significantly reduced in thapsigargin vs. controls at all distances d from the photodamage site (Figure 4 E(ii,iii), Figure S11 F, G, F', G').

Role connexin HCs and pannexin 1 channels

Open connexin HCs mediate the diffusive release of paracrine messengers, most importantly ATP.[60–64] Also pannexin 1 (Panx1) channels[65] are permeable to ATP,[66] expressed in the epidermis and important for differentiation of keratinocytes and wound healing.[67] In addition, Panx1 channels can be activated by extracellular ATP acting through purinergic receptors of the P2Y group, as well as by cytoplasmic Ca^{2+}.[68] Therefore, a positive-feedback loop involving the control by cytoplasmic Ca^{2+} of Panx1[68] and/or connexin HCs[42,69,70] may lead to an overall augmented ATP-induced ATP-release[68,71] that would increase both the area invaded by Ca^{2+} waves and the $[Ca^{2+}]_c$ increments in individual keratinocytes. Testing these hypotheses required further pharmacological interventions, as summarized hereafter.

Carbenoxolone (CBX) is a broad-spectrum inhibitor of connexin-made channel (i.e. HCs and IGJCs)[72] that inhibits also Panx1 channels[65,66] and IP_3-dependent Ca^{2+} release from the ER.[73] We injected 4 μl of VS containing CBX (400 μM), which reduced significantly both the area A(t) invaded by Ca^{2+} waves following focal photodamage (Figure S12 A, A') and the $\Delta F(t)/F_0$ responses in all bystander keratinocytes, except those adjected to the photodamage site (Figure S12 D, D'). The parameters a_{20s}, I and s were significantly reduced by CBX compared to controls at $d > 10\ \mu m$, and the arrest distance d_{stop} decreased by 20 μm with respect to control conditions (Figure 4F, Figure S12 E-G, E'-G').

To discriminate between Panx1 and connexin-made channels, we microinjected 4 μl of VS containing 4 mM of probenecid, which affects primarily Panx1 channels.[74] Probenecid modified slightly the time course of the equivalent radius $R(t)$ without affecting significantly the area invaded by the Ca^{2+} waves at their maximal expansion (Figure S13 A, A'). In addition, $\Delta F(t)/F_0$ signals were largely unaffected, with the exception of bystander keratinocytes located at $40\ \mu m \le d \le 50\ \mu m$ where responses appeared increased rather than decreased by the drug (Figure S13 D, D'). Only in this range of distances, the parameters a_{20s}, I and s were significantly larger in probenecid compared to controls, and the arrest distance d_{stop} was not affected (Figure 4G, Figure S13 E-G, E'-G'). These experiments lead us to conclude that (i) Panx1 channels were not involved in the Ca^{2+} signaling triggered by focal photodamage and (ii) the effect of CBX may reflect inhibition of connexin-made channel[72] and/or IP_3-dependent Ca^{2+} release from the ER.[73]

Various expression profiles of connexins through epidermis layers are reported in the literature, the majority of them agreeing in the predominance of Cx43 in the basal layer of the epidermis.[75–86] To discriminate between connexin HCs and IGJCs, we microinjected 4 μl of VS containing 200 μM TAT-Gap19, a peptide that selectively inhibits Cx43 HCs.[87] TAT-Gap19 did not change significantly the area invaded by Ca^{2+} waves (Figure S14 A, A'), whereas $\Delta F(t)/F_0$ signals in bystander keratinocytes were attenuated at larger distances (60, 70 μm) (Figure S14 D, D') compared to controls. The parameters a_{20s}, I and s were significantly reduced by Tat-Gap19 compared to controls at $d > 50\ \mu m$, but the arrest distance d_{stop} was not affected (Figure 4H, Figure S14 E-G, E'-G').

Comparison of experimental results with mathematical model

To overcome the limitations of pharmacological dissection, gain further mechanistic insight into these photodamage-evoked Ca^{2+} waves and determine whether the conclusions drawn from the experimental results can be reproduced coherently, we formulated a mathematical model (see Methods). To solve the system of model differential equations numerically, we assumed radial symmetry and reduced the problem to one dimension (see Methods). Considering the inter-animal variation (Figures S6-S14) the model with the chosen parameters (Table 3) reproduced well the experimental traces averaged over all control experiments (Figure 5A).

In the model, the simulated $\Delta F/F_0$ signal raised rapidly close to the damaged cell, followed by gradually more shallow and delayed responses at greater distances. The maximum model responses were achieved within 1–2 minutes after photodamage, thereafter $\Delta F/F_0$ signals slowly returned towards baseline on a timescale of more than 20 minutes for the cells closest to the damage site (Figure 5B). In other words, the simulations show a propagating wave that halts at approximately 80 μm from the damaged cell (Figure 5A) in agreement with the experiments, and with an equivalent radius (i.e., location of 30% response) as a function of time that mimics the experimental behavior (Figure 5C), in particular making allowance for the variability between different experimental animals (Figure S17). The model wave then slowly dissipated so that the equivalent radius reduced to 10 μm after about 18 min (Figure 5D).

After photodamage, the relatively large amounts of ATP present in the cytosol of the damaged cell diffused into the tight intercellular space. Near the damaged cells, the model ATP concentration reached tens to hundreds of μM (Figure 6A, B), hence the IP_3 producing machinery was completely saturated by ATP (the EC_{50} parameter in the model is $K_{PLC} = 1.05$ μM). As a result of the saturation of IP_3 production near the damaged cell, steady-state IP_3 levels are very similar at d <50 μm (Figure 6C). The long-lived responses with a duration of tens of minutes (Figure 5B) are due to the high ATP concentrations, which decrease only slowly over time due to the modest degradation rate and relatively low effective diffusion constant, D. We used $D = 65\ \mu m^2/s$, which is substantially lower than the diffusion constant of ATP in solution (350–400 $\mu m^2/s$).[88] However, the extracellular space between adjacent cells is about 20 nm,[40] i.e., only an order of magnitude larger than an ATP molecule, and is likely a crowded environment, which may slow down diffusion of ATP.[89] Indeed, the intracellular diffusion coefficient of ATP is ~3.5 times lower

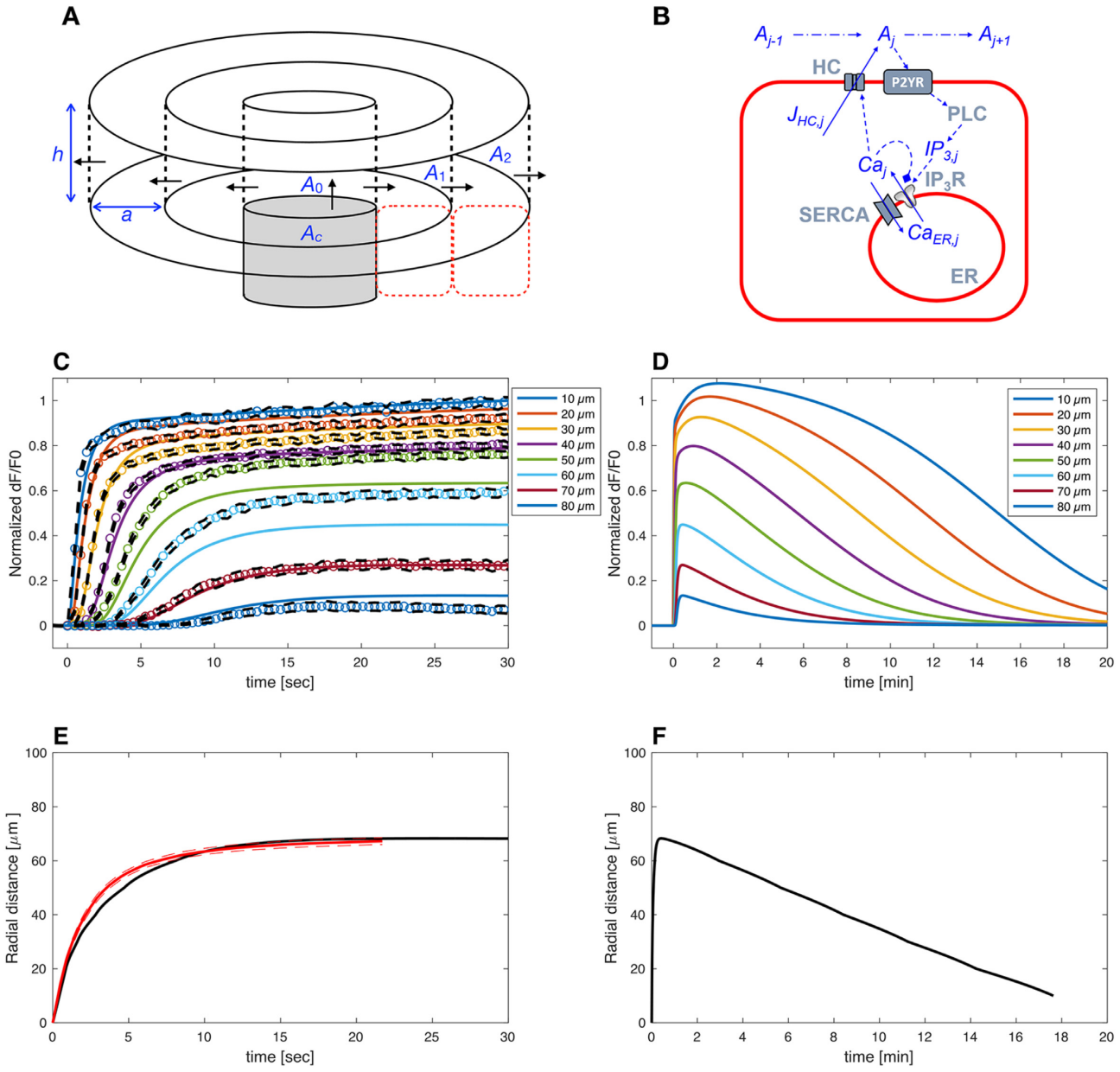

Figure 5. Model simulations for GCaMP6s fluorescence responses and equivalent radius of the area invaded by Ca^{2+} waves under control condition. (**A**) Schematic representation of model geometry. ATP dynamics is simulated as being released from the photodamaged cell (grey cylinder; A_c) into a thin disc above the cell (A_0). ATP diffusion in the intercellular space is simulated by discretizing in the radial direction assuming radial symmetry. The ATP concentration in each ring (A_j) communicates with the cells above and below (indicated by the red dashed rectangles). (**B**) Cartoon representing main actors of Ca^{2+} signaling in this model. HC, connexin hemichannels; SERCA, sarco-endoplasmic reticulum Ca^{2+} ATPases; IP_3R, inositol (1,4,5) triphosphate receptors; PLC, phospholipases C; $IP_{3,j}$, flux of IP_3; Ca_j, flux of ionized calcium out of endoplasmic reticulum (ER) through IP_3R; A_j, extracellular ATP concentration; $J_{HC,j}$, flux of ATP via connexin HCs; $Ca_{ER,j}$, flux of ionized calcium into the ER through SERCA; solid arrows represent net fluxes; dash-dotted arrows represent extracellular diffusion down the concentration gradient; dashed lines represent interactions: arrowheads for stimulatory interactions, diamond for inhibitory interaction. A_j stimulates IP_3 production via PLCβ. IP_3 in turn stimulates Ca^{2+} release from the ER via IP_3Rs. Intracellular Ca^{2+} is assumed to stimulate ATP release via HC and to stimulate PLC. In addition, Ca^{2+} feeds back onto IP_3R, and is pumped into the ER via SERCA pumps. (**C**) Simulated GCaMP6s $\Delta F(t)/F_0$ responses at increasing distances, in 10 μm steps, from the center of the damaged cell. Circles show the experimental results at the same distance as indicated by identical colors and specified in the legend. The black dashed curves show s.e.m of the experimental data points. (**D**) The simulation from panel **C** is shown here on an extended time scale to include the waning phase of the Ca^{2+} wave (note change of units from seconds to minutes in the abscissae). (**E**) Radius of the equivalent Ca^{2+} wave vs. time computed as the distance at which the response is 30% of the simulated response in panel **C** (black). The red curve shows corresponding experimental data with s.e.m. indicated by the dashed curves. (**F**) The simulation from panel **E** is shown here on an extended time scale to include the waning phase of the Ca^{2+} wave.

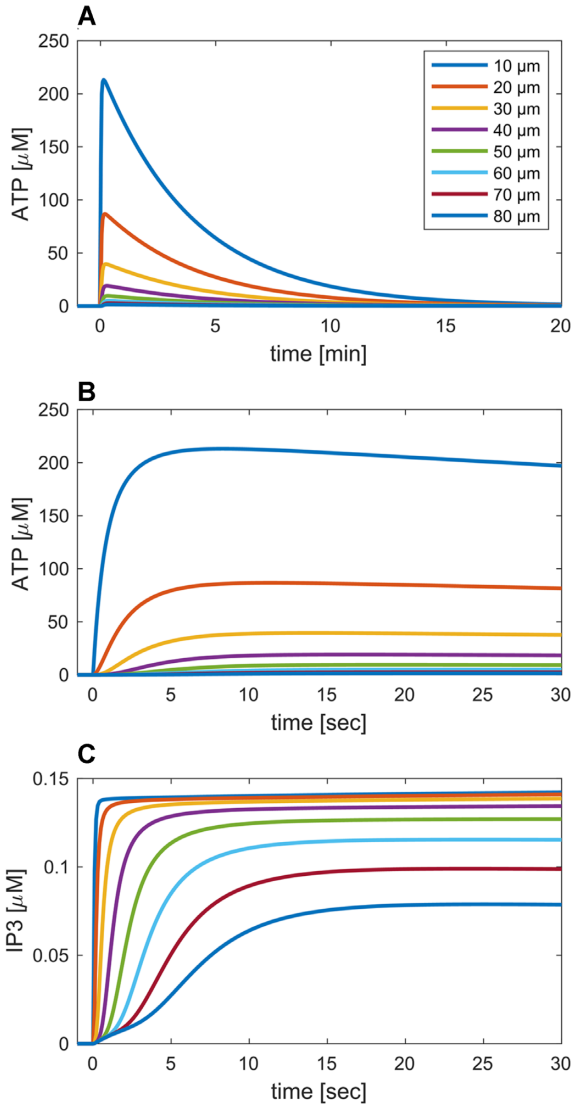

Figure 6. Model simulations for the concentrations of extracellular ATP and intracellular IP_3 under control conditions. (**A**) Simulated extracellular ATP responses at increasing distances, in 10 μm steps, from the center of the damaged cell as indicated by the color codes in the legend. (**B**) First 30 sec of the traces plotted in panel **A**. (**C**) Simulated intracellular IP_3 concentrations at increasing distances in the first 30 sec post damage and in 10 μm steps from the center of the damaged cell (traces color coded as in panel **A**).

than the extracellular value.[90] Further, ATP is buffered as it binds to e.g. ectonucleotidases, P2YRs and P2XRs on the cell membranes, and it is well-known that fixed buffers can reduce the effective diffusion constant substantially.[91]

The slowly increasing Ca^{2+} concentrations seen in the experiments even at very low distances are reproduced by the model because of slow feedback from cytosolic Ca^{2+} on PLC activity.[43–47] Note that this behavior cannot be explained by increased ATP levels, for example due to release from HCs, since any further increase in ATP beyond saturation would not lead to a raise in IP_3 and downstream $[Ca^{2+}]_c$ levels. Simulating increased ATP degradation, as in the apyrase experiments, reduced the $\Delta F/F_0$ model responses substantially at d >10 μm, and response were basically suppressed at d >30 μm (Figure 7A). The lack of model Ca^{2+} responses follows from the greatly reduced ATP levels at all distances (Figure 7B). Consequently, the waves stopped at 20–30 μm from the damaged cell (Figure 7C). In contrast, reducing the rate of ATP consumption to mimic the ARL experiments yielded larger $\Delta F/F_0$ model responses, in particular at larger distances (Figure 7D). The increased model ATP levels seen at all distances (Figure 7E) affected the cells at greater distances more, since their IP_3 production was far from saturation. Quantifying, the simulation corresponding to the ARL experiments shows a greater equivalent radius than the control simulation, corresponding to waves that terminate at ~100 μm (Figure 7F). Together, these model results show that the effects of apyrase and ARL can be explained entirely by interference with extracellular ATP degradation, which controls the extent of extracellular ATP levels.

Inhibition of connexin HCs, mimicking the TAT-Gap19 experiments, reduced the model responses at larger distances compared to the control scenario (Figure 8A), in agreement with experiments. Model cells with closed HCs did not release ATP, hence the extracellular ATP levels decreased (Figure 8B) causing a drop in IP_3 production and Ca^{2+} release from the ER. In control conditions, ATP release from HCs was larger close to the damaged cell since the $[Ca^{2+}]_c$was higher there than further away. However, the extracellular ATP was already saturating even without the contribution from the HCs, so blocking them had virtually no effect on $[Ca^{2+}]_c$variations at short distances from the photodamaged cell. On the contrary, at larger distances the contribution to extracellular ATP from HCs was relatively important compared to the ATP diffusion from the site of damage. Consequently, inhibiting HCs has a substantial effect on the simulated response. This explains why HCs blockade lowered the extent of wave propagation in the model (Figure 8C). Increasing the maximal rate of IP_3 production, V_{PLC}, yielded simulated responses that resembled the experimental data with zero extracellular Ca^{2+} and EGTA. At all distances, importantly also at the shortest distances from the damaged cell, the $\Delta F/F_0$ signals increased (Figure 8D) partly because of the positive feedback from Ca^{2+} on ATP release from HCs, which increased ATP levels at the larger distances (Figure 8E). Consequently, the wave propagated ~10 μm further than in control simulations (Figure 8F).

Discussion

We have shown here that ATP is released from epidermal keratinocytes of live anesthetized mice following intradermal photodamage caused by intense pulsed IR laser radiation. Kumamoto *et al.* obtained results compatible with those reported here using point laser stimulation of keratinocytes in *ex vivo* human epidermis. In particular, they observed different responses in the various layers of the epidermis after stimulating a keratinocyte of the *stratum granulosum*, with higher responses in the basal layer.[13]

Insight provided by *in vivo* pharmacological dissection experiments

The largest effects were caused by drugs that interfere with degradation of extracellular ATP or P2 purinoceptors, suggesting that Ca^{2+} waves in the photodamaged epidermis are primarily due to release of ATP from the target cell whose plasma membrane integrity was compromised by laser irradiation. As $\Delta F(t)/F_0$ signals in bystander keratinocytes were augmented by exposure to the Ca^{2+} chelator EGTA in the extracellular medium, the corresponding transient increments of the $[Ca^{2+}]_c$ should be ascribed primarily to Ca^{2+} release from the ER, downstream of ATP binding to P2Y purinoceptors with Ca^{2+} entry through

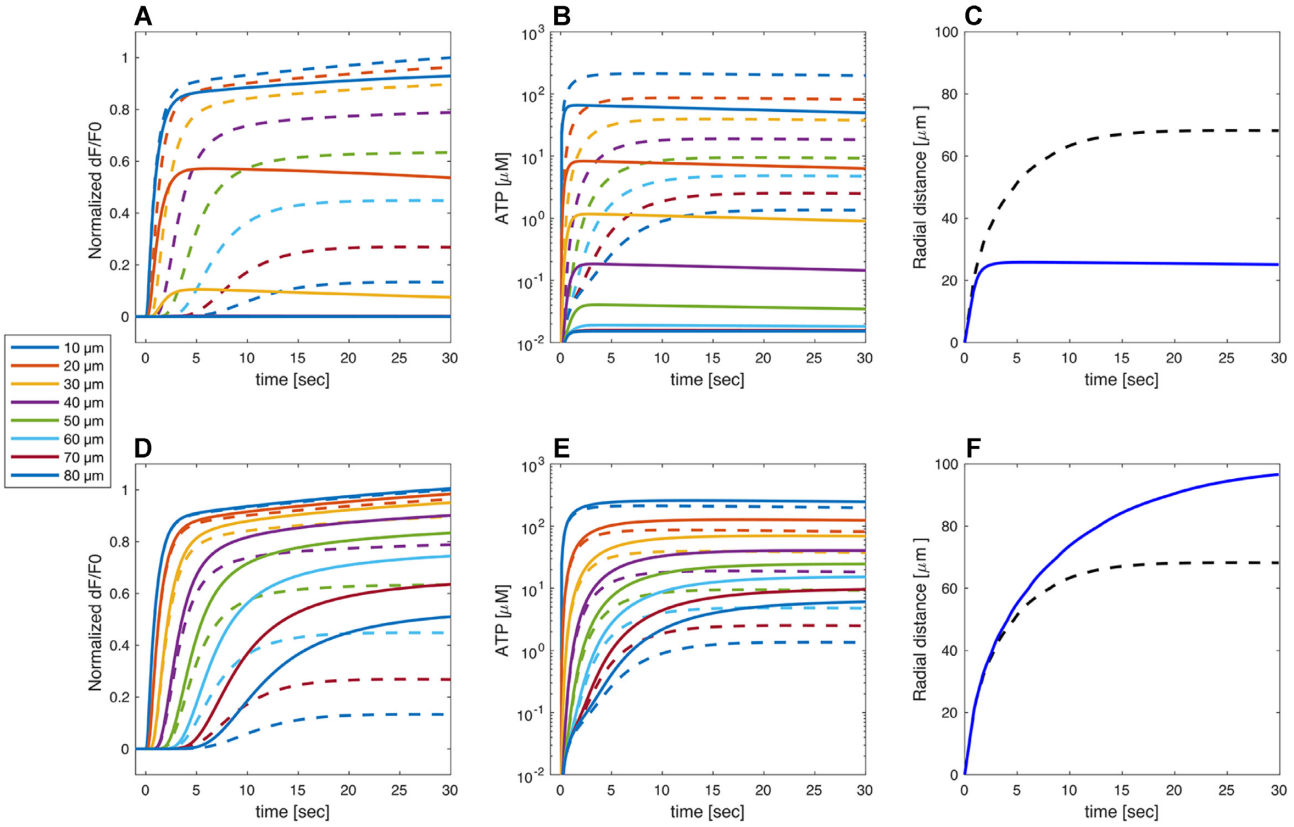

Figure 7. Model simulation of interference with extracellular ATP handling. (**A-C**) Simulated apyrase experiment performed by increasing 10-fold the ATP degradation rate *k* (full curves). The simulations under control conditions (from Figures 5 and 6) are shown for comparison as dashed curves with the same color code. (**A**) Simulated normalized GCaMP6s fluorescence responses, as indicated by the color codes in the legend. (**B**) Model extracellular ATP levels. (**C**) Equivalent radii from apyrase (blue solid line) and control (black dashed line, same as black solid line in Figure 5E) simulations. (**D-F**) Simulated ARL experiment performed by decreasing the ATP degradation rate *k* by 50% (solid lines). Legends as in panels **A-C**. Traces in panels **A**, **B**, **D**, **E** were computed at increasing distances, in 10 μm steps, from the center of the damaged cell.

plasma membrane channels playing a comparatively negligible role. The effect of thapsigargin supports this conclusion.

PPADS antagonizes $P2Y_1$,[92] $P2Y_4$,[93] $P2Y_6$[94] and $P2Y_{13}$[95] receptors (see also ref.[29]). In contrast, $P2Y_2$Rs are PPADS-insensitive.[29,93] Published work on P2Y mRNA expression in murine keratinocytes identified $P2Y_1$R, $P2Y_2$R, $P2Y_4$R and $P2Y_6$R subtypes,[96] therefore $P2Y_2$Rs are likely responsible for the incomplete effect of PPADS administration.

The ineffectiveness of probenecid suggests pannexin channels had no role, whereas the limited effect of TAT-Gap19 suggests ATP-dependent ATP release though connexin HCs affected Ca^{2+} wave propagation only at larger distances, where the concentration of ATP released from the photodamaged cell was reduced by the combined effect of passive diffusion and hydrolysis due to the action of ecto-ATPases. The fact that CBX exerted a stronger inhibitory action compared to TAT-Gap19 may suggest that IGJCs played a more prevalent role than Cx43 HCs in Ca^{2+} wave propagation. However, CBX has been recently reported to interference also with IP_3Rs,[97] which would instead lend further support to a fundamental role played by the P2Y-dependent pathway and IP_3-dependent Ca^{2+} release from intracellular stores.

Insight provided by the mathematical model

Our mathematical model reproduced the experimental observations by assuming that extracellular ATP diffusion carried the signal from the damaged to bystander cells, where it activated PLC and increased IP_3 levels, which in turn triggered Ca^{2+} release via IP_3Rs. Ca^{2+} feedback onto PLC caused the slowly rising response during the expansion phase of the Ca^{2+} waves. Close to the damaged cell, ATP concentrations were saturating for the P2YRs/PLC machinery, whereas the wave stopped further away where degradation and dilution of ATP lowered the ATP concentration to levels insufficient to cause substantial Ca^{2+} release. Changes in the model degradation rate reproduced experiments with apyrase and ARL. ATP release through connexin HCs contributed comparatively more at longer distances, where the flux of ATP from cytosol raised the extracellular ATP levels sufficiently to yield an intracellular Ca^{2+} response. However, HCs contribution was eclipsed in the proximity of the damage site by the far preponderant contribution from photodamage.

We also propose a plausible explanation for how chelation of extracellular Ca^{2+} with EGTA might increase PLC activity. In keratinocytes, extracellular Ca^{2+} partly activates PKC,[98] thus removal of extracellular Ca^{2+} may ensue in a reduced PKC activity. Since PKC inhibits PLC,[44,99,100] PKC deactivation would remove the brake on the rate of IP_3 production. Note that alternative explanations invoking an increase in extracellular ATP levels following chelation of extracellular Ca^{2+}, for example because of a direct effect of low Ca^{2+} on connexin HCs, are incompatible with the saturating ATP levels near the damaged cell.

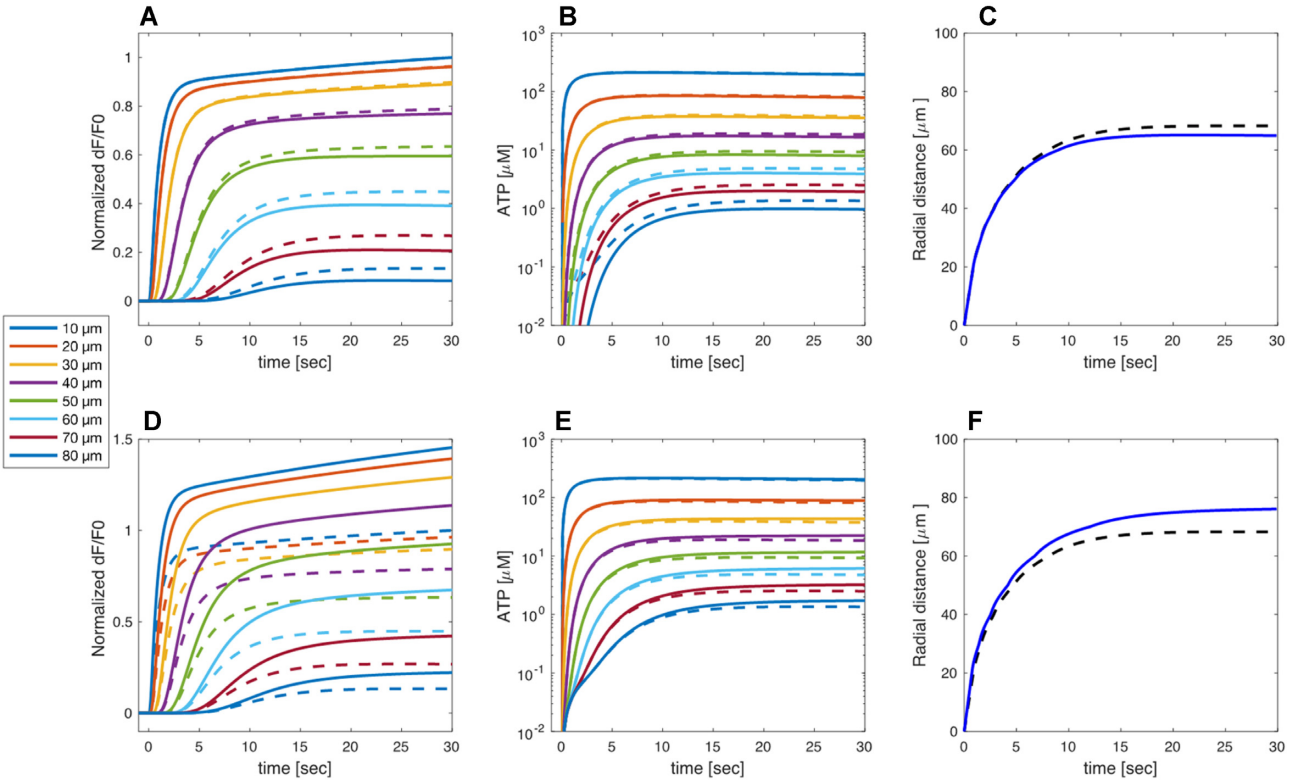

Figure 8. Model simulation of connexin HCs inhibition and extracellular Ca $^{2+}$ chelation. (**A-C**) Simulated TAT-Gap19 experiment performed by decreasing the rate of ATP release through connexin HCs (full curves). The simulations under control conditions (from Figures 5 and 6) are shown for comparison as dashed curves with the same color code. (**A**) Simulated normalized GCaMP6s fluorescence responses, as indicated by the color codes in the legend. (**B**) Model extracellular ATP levels. (**C**) Equivalent radii from TAT-Gap19 (blue solid line) and control (black dashed line, same as black solid line in Figure 5E) simulations. (**D-F**) Simulated EGTA experiment performed by increasing the maximal rate of IP_3 production V_{PLC} by 7% (see main text). Legends as in panels **A-C**. Traces in panels **A**, **B**, **D**, **E** were computed at increasing distances, in 10 μm steps, from the center of the damaged cell.

In the proposed model, we neglected intercellular Ca^{2+} and IP_3 diffusion via inter-cellular gap junction channels since our experiments suggested that extracellular ATP diffusion is the major route of signal propagation, in contrast to other physiological systems (e.g. Refs[101–103]). Thus, in our model, the waves are propagating with no communication between the bystander cells, except from a near-negligible contribution due to ATP diffusion through hemichannels.

The mechanism for wave block of the simulated abortive waves that we studied here differs from – but also has similarities to – other systems. For example, in gap-junction coupled pancreatic beta-cells, an externally imposed glucose gradient causes abortive, repetitive Ca^{2+} waves,[104,105] which have been proposed to stop because of the gradual reduction in excitability of the cells,[106,107] resembling the ATP gradient observed here, although the waves between beta-cells are driven by electrical communication via gap junctions. Heterogeneity in cellular and gap-junction properties in combination with discretization effects may also lead to propagation failure between coupled cells.[108–111] Such heterogeneity was not considered here, and the model waves stop simply when the concentration of diffusing ATP becomes too low to stimulate sufficient IP_3 production to increase the intracellular Ca^{2+} concentration.

The observed near-steady and long-lived $[Ca^{2+}]_c$ elevations were quantitatively different from the $[Ca^{2+}]_c$ oscillations often observed, for example, in the sensory epithelium of the cochlea following photodamage[11,12] or IP_3 uncaging.[71,112–114] Why are such oscillations not seen in the photodamaged skin? Also in this case, the mathematical model provides a possible explanation. The core of the Ca^{2+} signaling part of the model is the Li-Rinzel model,[48] which is well-known to sustain oscillations, but only for a range of IP_3 concentrations. We therefore investigated how the single-cell model depends on the IP_3 production rate V_{PLC} (assuming that ATP levels were saturating). The bifurcation diagram in Figure 9 shows that the model has a single stable equilibrium at low V_{PLC} values, which becomes unstable due to a subcritical Hopf bifurcation at $V_{PLC} = 2.02$. The equilibrium becomes stable again for values above $V_{PLC} = 2.44$, where another subcritical Hopf bifurcation occurs. The unstable limit cycles born in the Hopf bifurcations become stable at saddle-node of limit cycles bifurcations, thus the model generates stable oscillations for values of V_{PLC} between 2.0 and 2.45 (approximately). Hence, the default value of $V_{PLC} = 1.85$, which we used to reproduce the experiments, is too low to sustain oscillations. Biologically, this explanation corresponds to the hypothesis that keratinocytes have too few P2YRs and/or amounts of PLC to transduce the high ATP levels into sufficiently high rates of IP_3 production to cause $[Ca^{2+}]_c$ oscillations.

Significance of the present findings for skin therapy and wound healing

In laser skin resurfacing with intra-epidermal focal laser-induced photodamage, the targeted micro-regions are thought to promote formation of new dermal collagen and elastin during the repair process,[32–35] but the underlying mechanisms were

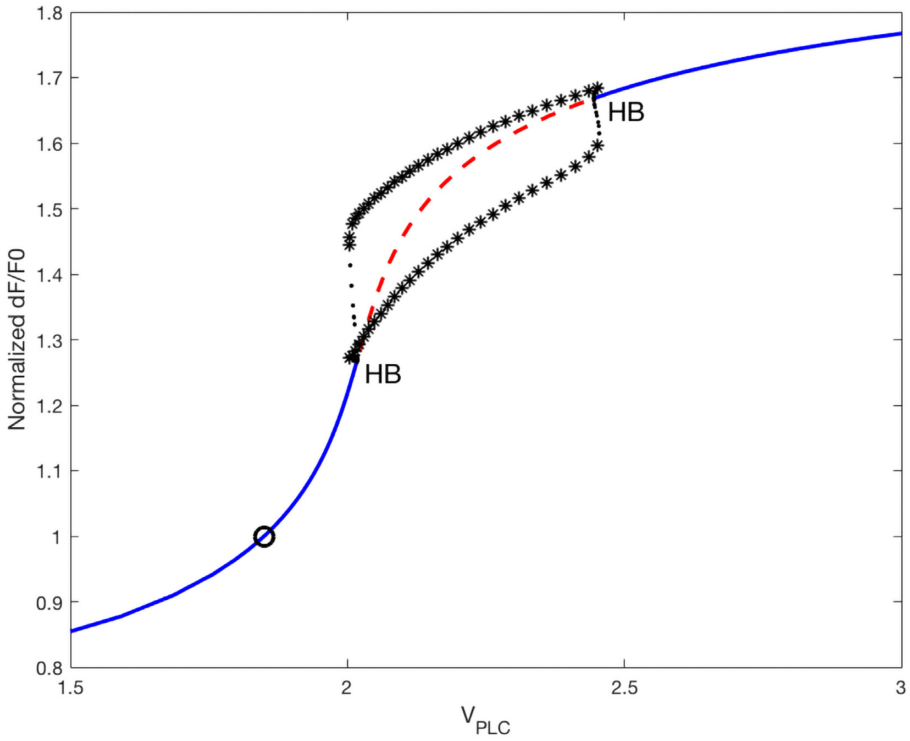

Figure 9. Bifurcation diagram of the single-cell model. The steady-state $\Delta F(t)/F_0$ response, normalized to the response at the default value of V_{PLC}= 1.85 μM/s, is shown as a function of the maximal rate of IP_3 production, V_{PLC}, under the assumption of saturating ATP levels. At low V_{PLC} values, the steady-state is stable (blue solid line), but loses stability in a Hopf bifurcation (HB) at V_{PLC}≈2.02. The unstable fixpoint (red dashed line) regains stability in another HB at V_{PLC}≈2.44. Unstable limit cycles (black asterisks) are born at both HBs, but due to saddle-node-of-limit-cycles bifurcations at V_{PLC}≈2.0 and V_{PLC}≈ 2.45, stable limit cycles are present between these values. The black circle indicates the default value of V_{PLC} used in the model, which is located below the interval where the system may oscillate.

poorly understood before this study. Our results clearly indicate that P2YRs are activated by ATP downstream of photodamage, and P2YRs regulate cell proliferation, differentiation and migration,[115–117] besides being involved in wound healing.[31] A prime target of the associated signaling activity is likely to be the extracellular matrix (ECM). In cultured keratinocytes, ATP caused a rapid and strong but transient activation of hyaluronan synthase 2 (*HAS2*) expression (via PKC-, CaMKII-, MAPK- and CREB-dependent pathways) by activating $P2Y_2$Rs.[118] Hyaluronan, also named hyaluronic acid, is a major component of the ECM, and its synthesis is rapidly upregulated after tissue wounding.[119] Thus, epidermal insults are associated with extracellular ATP release, as well as hyaluronan synthesis, and the two phenomena are linked.[118]

In addition, ATP is well known as one of the DAMPs that, once released from injured cells, activate the immune system.[120] Besides alerting the body about danger and initiate the immune response, DAMPs also promote regeneration processes.[120] P2YRs are important also in this context, because they regulate many aspects of immune cell function, including phagocytosis and killing of pathogens, antigen presentation, chemotaxis, degranulation, cytokine production, and lymphocyte activation.[121] In the epidermis, Langerhans cells, characterized by the expression of Langerin (CD207) and CD1a, are considered to be macrophages that retain the function of dendritic cells, playing a clear role of antigen-presenting cells in skin inflammation, triggering a series of immune responses by migrating from the epidermis to the lymph nodes and presenting antigens to T-regulatory cells.[122] A Langerhans cell line (XS106) was shown to express mRNA for $P2X_1$, $P2X_7$, $P2Y_1$, $P2Y_2$, $P2Y_4$, and $P2Y_{11}$ receptors,[123] which is consistent with the increase in GCaMP6s fluorescence in Langerhans cells we observed in some of our *in vivo* experiments. Therefore, it would be interesting, in future studies, to trace the movements of the Langerhans cells invested by damage-evoked Ca^{2+} waves.

In our experimental model, Ca^{2+} waves reached into the fibroblast-populated collagen matrix, and this event may activate and coordinate the keratinocyte-fibroblast interaction that is key to wound healing and skin remodeling.[124,125] Indeed, fibroblasts are well known not only for being the major producers of extracellular matrix, but also as a cell type actively involved in synthesis of inflammatory mediators and tissue repair. ATP or UTP increased the levels of ECM-related proteins through the activation of $P2Y_2$Rs in mouse fibroblasts.[126] Therefore, it is tempting to speculate that response coordination after accidental injury or laser treatment occurs via propagation of the ATP-dependent Ca^{2+} waves we visualized and analyzed in this article.

Concluding remarks

Numerous other molecular players contribute to epidermal Ca^{2+} homeostasis, therefore Ca^{2+} dynamics may involve a variety of other processes we did not take into account, including Ca^{2+}-sensing receptor, transient receptor potential channels, store-operated calcium entry channel Orai1, endoplasmic Ca^{2+} depletion sensor (stromal interaction molecule 1 [STIM1]), and voltage-gated calcium channels such as L-type calcium channels.[18,127] In addition, further experiments are required to better characterize the dynamics of ATP after it is released into the extracellular space and is degraded rapidly to ADP, AMP, and

further to adenosine,[64] which (with the exception of AMP) activate specific receptors even in a self-sustaining fashion.[128]

Supplementary Material

Supplementary material is available at the *APS Function* online.

Data and code availability

Data were archived in a repository handled by the University of Padova and can be accessed at: http://researchdata.cab.unipd.it/id/eprint/547.

The model code is available in the repository managed by the University of Padova at http://researchdata.cab.unipd.it/id/eprint/559 and at http://www.dei.unipd.it/~pedersen.

The roiSelection GUI code is available on GitHub at https://github.com/DonatiViola/ROISELECTION.git.

Author contributions

Conceptualization: F.M. ***Data Curation:*** V.D., C.P. ***Formal Analysis:*** V.D., C.P. ***Funding Acquisition:*** F.M. ***Investigation:*** V.D., C.P., C.N. ***Methodology:*** M.B., M.G.P. ***Project Administration:*** F.M. ***Resources:*** F.M., F.S., M.R. ***Software:*** F.M., C.D.C., V.D., C.P., M.B., M.G.P. ***Supervision:*** F.M., M.B.

Validation: V.D., C.P. C.N. ***Visualization:*** V.D., C.P., M.B., M.G.P. ***Writing - Original Draft Preparation:*** F.M. ***Writing - Review and Editing:*** F.M., V.D., C.P., C.N., M.B., M.G.P.

Funding

This work was supported by the University of Padova (Grant No. BIRD187130 to FM) and Fondazione Telethon (Grant No. GGP19148 to FM). The funders had no role in study design, data collection, data analysis, interpretation or writing of the report.

Conflict of interest statement

The authors declare no competing interests.

References

1 McGrath JA, Eady RAJ, Pope FM. Anatomy and Organization of Human Skin. *Rook's Textbook of Dermatology*, 2004. doi:0.1002/9780470750520.ch3.

2 Koster MI. Making an epidermis. *Ann N Y Acad Sci* 2009;**1170**(1):7–10.

3 Watt FM. Stem cell fate and patterning in mammalian epidermis. *Curr Opin Genet Dev* 2001;**11**:410–417.

4 Alonso L, Fuchs E. Stem cells of the skin epithelium. *Proc Natl Acad Sci* 2003;**100**(Supplement 1):11830–11835.

5 Blanpain C, Lowry WE, Geoghegan A, Polak L, Fuchs E. Self-renewal, multipotency, and the existence of two cell populations within an epithelial stem cell niche. *Cell* 2004;**118**(5):635–648.

6 Horsley V, et al. Blimp1 defines a progenitor population that governs cellular input to the sebaceous gland. *Cell* 2006;**126**(3):597–609.

7 Blanpain C, Fuchs E. Epidermal homeostasis: a balancing act of stem cells in the skin. *Nature reviews. Molecular cell biology* 2009;**10**:207–217.

8 Fuchs E. In *Current Topics in Developmental Biology*Vol. **116**, ed Wassarman P M. 357–374 Academic Press, Cambridge, MA. 2016.

9 Boitano S, Dirksen ER, Sanderson MJ. Intercellular propagation of calcium waves mediated by inositol trisphosphate. *Science* 1992;**258**(5080):292–295.

10 Klepeis VE, Cornell-Bell A, Trinkaus-Randall V. Growth factors but not gap junctions play a role in injury-induced Ca2+ waves in epithelial cells. *J Cell Sci* 2001;**114**(23):4185–4195.

11 Gale JE, Piazza V, Ciubotaru CD, Mammano F. A mechanism for sensing noise damage in the inner ear. *Curr Biol* 2004;**14**(6):526–529.

12 Mazzarda F, et al. Organ-on-chip model shows that ATP release through connexin hemichannels drives spontaneous Ca(2+) signaling in non-sensory cells of the greater epithelial ridge in the developing cochlea. *Lab Chip* 2020;**20**(16):3011–3023.

13 Kumamoto J, Goto M, Nagayama M, Denda M. Real-time imaging of human epidermal calcium dynamics in response to point laser stimulation. *J Dermatol Sci* 2017;**86**(1):13–20.

14 Handly LN, Wollman R. Wound-induced Ca(2+) wave propagates through a simple release and diffusion mechanism. *Mol Biol Cell* 2017;**28**(11):1457–1466.

15 Leybaert L, Sanderson MJ. Intercellular Ca2+ waves: mechanisms and function. *Physiol Rev* 2012;**92**(3):1359–1392.

16 Elias P, Ahn S, Brown B, Crumrine D, Feingold KR. Origin of the epidermal calcium gradient: regulation by barrier status and role of active vs passive mechanisms. *J Invest Dermatol* 2002;**119**(6):1269–1274.

17 Elias PM, et al. Modulations in epidermal calcium regulate the expression of differentiation-specific markers. *J Invest Dermatol* 2002;**119**(5):1128–1136.

18 Lee SE, Lee SH. Skin Barrier and Calcium. *Annals of dermatology* 2018;**30**(3):265–275.

19 Michaletti A, et al. Multi-omics profiling of calcium-induced human keratinocytes differentiation reveals modulation of unfolded protein response signaling pathways. *Cell Cycle* 2019;**18**(17):2124–2140.

20 Dhitavat J, et al. Mutations in the sarcoplasmic/endoplasmic reticulum Ca2+ ATPase isoform cause Darier's disease. *J Invest Dermatol* 2003;**121**(3):486–489.

21 Burnstock G. Purinergic nerves. *Pharmacol Rev* 1972;**24**:509–581.

22 Giuliani AL, Sarti AC, Di Virgilio F. Extracellular nucleotides and nucleosides as signalling molecules. *Immunol Lett* 2019;**205**:16–24.

23 Barr TP, et al. Air-stimulated ATP release from keratinocytes occurs through connexin hemichannels. *PLoS One* 2013;**8**(2):e56744.

24 Takahashi T, et al. In vivo imaging demonstrates ATP release from murine keratinocytes and its involvement in cutaneous inflammation after tape stripping. *J Invest Dermatol* 2013;**133**(10):2407–2415.

25 Koizumi S, et al. Ca2+ waves in keratinocytes are transmitted to sensory neurons: the involvement of extracellular ATP and P2Y2 receptor activation. *Biochem J* 2004;**380**(2):329–338.

26 Takada H, Furuya K, Sokabe M. Mechanosensitive ATP release from hemichannels and Ca(2)(+) influx through TRPC6 accelerate wound closure in keratinocytes. *J Cell Sci* 2014;**127**:4159–4171.

27 Boukamp P, et al. Normal keratinization in a spontaneously immortalized aneuploid human keratinocyte cell line. *J Cell Biol* 1988;**106**(3):761–771.
28 Khakh BS, North RA. P2X receptors as cell-surface ATP sensors in health and disease. *Nature* 2006;**442**(7102):527–532.
29 Abbracchio MP, et al. International Union of Pharmacology LVIII: update on the P2Y G protein-coupled nucleotide receptors: from molecular mechanisms and pathophysiology to therapy. *Pharmacol Rev* 2006;**58**(3):281–341.
30 Erb L, Weisman GA. Coupling of P2Y receptors to G proteins and other signaling pathways. *Wiley Interdisciplinary Reviews: Membrane Transport and Signaling* 2012;**1**(6):789–803.
31 Burnstock G, Knight GE, Greig AV. Purinergic signaling in healthy and diseased skin. *J Invest Dermatol* 2012;**132**(3):526–546.
32 Orringer JS, et al. Intraepidermal erbium:YAG laser resurfacing: impact on the dermal matrix. *J Am Acad Dermatol* 2011;**64**(1):119–128.
33 Tanghetti EA. The histology of skin treated with a picosecond alexandrite laser and a fractional lens array. *Lasers Surg Med* 2016;**48**(7):646–652.
34 Balu M, et al. In vivo multiphoton-microscopy of picosecond-laser-induced optical breakdown in human skin. *Lasers Surg Med* 2017;**49**(6):555–562.
35 Connor KO, Cho SB, Chung HJ. Wound Healing Profile After 1064- and 532-nm Picosecond Lasers With Microlens Array of In Vivo Human Skin. *Lasers Surg Med*, 2021. doi:10.1002/lsm.23390.
36 Chen T-W, et al. Ultrasensitive fluorescent proteins for imaging neuronal activity. *Nature* 2013;**499**(7458):295.
37 Kilkenny C, Browne WJ, Cuthill IC, Emerson M, Altman DG. Improving bioscience research reporting: the ARRIVE guidelines for reporting animal research. *Osteoarthritis Cartilage* 2012;**20**(4):256–260.
38 Smith AJ, Clutton RE, Lilley E, Hansen KEA, Brattelid T. PREPARE: guidelines for planning animal research and testing. *Lab Anim* 2018;**52**(2):135–141.
39 Mammano F, Bortolozzi M. In *Calcium Measurement Methods*Vol. 43, eds 57–80. Humana Press, Totowa, New Jersey. 2010.
40 Wolff K, Wolff-Schreiner EC. Trends in electron microscopy of skin. *J Invest Dermatol* 1976;**67**(1):39–57.
41 Crank J. *The Mathematics of Diffusion. second edn*, Oxford, UK, Oxford University Press, 1975.
42 De Vuyst E, et al. Intracellular calcium changes trigger connexin 32 hemichannel opening. *EMBO J* 2006;**25**(1):34–44.
43 Suh PG, et al. Multiple roles of phosphoinositide-specific phospholipase C isozymes. *BMB reports* 2008;**41**(6):415–434.
44 Punnonen K, et al. Keratinocyte differentiation is associated with changes in the expression and regulation of phospholipase C isoenzymes. *J Invest Dermatol* 1993;**101**(5):719–726.
45 Allen V, Swigart P, Cheung R, Cockcroft S, Katan M. Regulation of inositol lipid-specific phospholipase cdelta by changes in Ca2+ ion concentrations. *Biochem J* 1997;**327**(2):545–552.
46 Kim YH, et al. Phospholipase C-delta1 is activated by capacitative calcium entry that follows phospholipase C-beta activation upon bradykinin stimulation. *J Biol Chem* 1999;**274**(37):26127–26134.
47 Thore S, Dyachok O, Gylfe E, Tengholm A. Feedback activation of phospholipase C via intracellular mobilization and store-operated influx of Ca2+ in insulin-secreting beta-cells. *J Cell Sci* 2005;**118**(19):4463–4471.
48 Li YX, Rinzel J. Equations for InsP3 receptor-mediated [Ca2+]i oscillations derived from a detailed kinetic model: a Hodgkin-Huxley like formalism. *J Theor Biol* 1994;**166**(4):461–473.
49 Handa M, Guidotti G. Purification and cloning of a soluble ATP-diphosphohydrolase (apyrase) from potato tubers (Solanum tuberosum). *Biochem Biophys Res Commun* 1996;**218**(3):916–923.
50 Lambrecht G. Design and pharmacology of selective P2-purinoceptor antagonists. *J Auton Pharmacol* 1996;**16**(6):341–344.
51 Robson SC, Sevigny J, Zimmermann H. The E-NTPDase family of ectonucleotidases: Structure function relationships and pathophysiological significance. *Purinergic Signal* 2006;**2**(2):409–430.
52 Zuo P, et al. Mathematical model of nucleotide regulation on airway epithelia. Implications for airway homeostasis. *J Biol Chem* 2008;**283**(39):26805–26819.
53 Kukulski F, et al. Comparative hydrolysis of P2 receptor agonists by NTPDases 1, 2, 3 and 8. *Purinergic signalling* 2005;**1**(2):193–204.
54 Levesque SA, Lavoie EG, Lecka J, Bigonnesse F, Sevigny J. Specificity of the ecto-ATPase inhibitor ARL 67156 on human and mouse ectonucleotidases. *Br J Pharmacol* 2007;**152**(1):141–150.
55 Westfall TD, Kennedy C, Sneddon P. Enhancement of sympathetic purinergic neurotransmission in the guinea-pig isolated vas deferens by the novel ecto-ATPase inhibitor ARL 67156. *Br J Pharmacol* 1996;**117**(5):867–872.
56 Baqi Y. Ecto-nucleotidase inhibitors: recent developments in drug discovery. *Mini Rev Med Chem* 2015;**15**(1):21–33.
57 Raaflaub J. Applications of Metal Buffers and Metal Indicators in Biochemistry. *Methods Biochem Anal*, 1956;301–325.
58 Lee WK, et al. Purinoceptor-mediated calcium mobilization and proliferation in HaCaT keratinocytes. *J Dermatol Sci* 2001;**25**(2):97–105.
59 Lytton J, Westlin M, Hanley MR. Thapsigargin inhibits the sarcoplasmic or endoplasmic reticulum Ca-ATPase family of calcium pumps. *J Biol Chem* 1991;**266**(26):17067–17071.
60 Toma I, et al. Connexin 40 and ATP-dependent intercellular calcium wave in renal glomerular endothelial cells. *American Journal of Physiology-Regulatory, Integrative and Comparative Physiology* 2008;**294**(6):R1769–R1776.
61 Cotrina ML, et al. Connexins regulate calcium signaling by controlling ATP release. *Proc Natl Acad Sci* 1998;**95**(26):15735–15740.
62 Stout CE, Costantin JL, Naus CC, Charles AC. Intercellular calcium signaling in astrocytes via ATP release through connexin hemichannels. *J Biol Chem* 2002;**277**(12):10482–10488.
63 Pearson RA, Dale N, Llaudet E, Mobbs P. ATP released via gap junction hemichannels from the pigment epithelium regulates neural retinal progenitor proliferation. *Neuron* 2005;**46**(5):731–744.
64 Ho CL, Yang CY, Lin WJ, Lin CH. Ecto-nucleoside triphosphate diphosphohydrolase 2 modulates local ATP-induced calcium signaling in human HaCaT keratinocytes. *PLoS One* 2013;**8**(3):e57666.
65 Bruzzone R, Hormuzdi SG, Barbe MT, Herb A, Monyer H. Pannexins, a family of gap junction proteins expressed in brain. *Proc Natl Acad Sci* 2003;**100**(23):13644–13649.
66 Ruan Z, Orozco IJ, Du J, Lu W. Structures of human pannexin 1 reveal ion pathways and mechanism of gating. *Nature*,**584**,(7822):646–651, 2020.

67 Penuela S, et al. Panx1 regulates cellular properties of keratinocytes and dermal fibroblasts in skin development and wound healing. *J Invest Dermatol* 2014;**134**(7):2026–2035.

68 Locovei S, Wang J, Dahl G. Activation of pannexin 1 channels by ATP through P2Y receptors and by cytoplasmic calcium. *FEBS Lett* 2006;**580**(1):239–244.

69 Carrer A, et al. Cx32 hemichannel opening by cytosolic Ca2+ is inhibited by the R220X mutation that causes Charcot-Marie-Tooth disease. *Hum Mol Genet* 2018;**27**(1):80–94.

70 De Vuyst E, et al. Ca(2+) regulation of connexin 43 hemichannels in C6 glioma and glial cells. *Cell Calcium* 2009;**46**(3):176–187.

71 Ceriani F, Pozzan T, Mammano F. Critical role of ATP-induced ATP release for Ca2+ signaling in nonsensory cell networks of the developing cochlea. *Proc Natl Acad Sci* 2016;**113**(46):E7194–E7201.

72 Connors BW. Tales of a dirty drug: carbenoxolone, gap junctions, and seizures. *Epilepsy currents* 2012;**12**(2):66–68.

73 Buckley C, Zhang X, Wilson C, McCarron JG. Carbenoxolone and 18beta-Glycyrrhetinic acid inhibit IP3 -mediated endothelial cell calcium signalling and depolarise mitochondria. *Br J Pharmacol*, 2020. doi:10.1111/bph.15329.

74 Lohman AW, Isakson BE. Differentiating connexin hemichannels and pannexin channels in cellular ATP release. *FEBS Lett* 2014;**588**(8):1379–1388.

75 Garcia-Vega L, O'Shaughnessy EM, Albuloushi A, Martin PE. Connexins and the epithelial tissue barrier: a focus on connexin 26. *Biology* 2021;**10**(1):59.

76 Mese G, Richard G, White TW. Gap junctions: basic structure and function. *J Invest Dermatol* 2007;**127**(11):2516–2524.

77 Martin PE, Easton JA, Hodgins MB, Wright CS. Connexins: sensors of epidermal integrity that are therapeutic targets. *FEBS Lett* 2014;**588**(8):1304–1314.

78 Churko JM, Laird DW. Gap junction remodeling in skin repair following wounding and disease. *Physiology* 2013;**28**(3):190–198.

79 Wong P, et al. The role of connexins in wound healing and repair: novel therapeutic approaches. *Frontiers in physiology* 2016;**7**. doi:10.3389/fphys.2016.00596.

80 Wang X, Ramirez A, Budunova I. Overexpression of connexin26 in the basal keratinocytes reduces sensitivity to tumor promoter TPA. *Exp Dermatol* 2010;**19**(7):633–640.

81 Goliger JA, Paul DL. Expression of gap junction proteins Cx26, Cx31.1, Cx37, and Cx43 in developing and mature rat epidermis. *Dev Dyn* 1994;**200**(1):1–13.

82 Delmar M, et al. Connexins and disease. *Cold Spring Harb Perspect Biol*, 2017. doi:10.1101/cshperspect.a029348.

83 Faniku C, Wright CS, Martin PE. Connexins and pannexins in the integumentary system: The skin and appendages. *Cell Mol Life Sci* 2015;**72**(15):2937–2947.

84 Kandyba EE, Hodgins MB, Martin PE. A murine living skin equivalent amenable to live-cell imaging: analysis of the roles of connexins in the epidermis. *J Invest Dermatol* 2008;**128**(4):1039–1049.

85 Kretz M, et al. Altered connexin expression and wound healing in the epidermis of connexin-deficient mice. *J Cell Sci* 2003;**116**(16):3443–3452.

86 Maher AC, et al. Rat epidermal keratinocytes as an organotypic model for examining the role of Cx43 and Cx26 in skin differentiation. *Cell Commun Adhes* 2005;**12**:219–230.

87 Abudara V, et al. The connexin43 mimetic peptide Gap19 inhibits hemichannels without altering gap junctional communication in astrocytes. *Frontiers in cellular neuroscience* 2014;**8**:306.

88 Hubley MJ, Locke BR, Moerland TS. The effects of temperature, pH, and magnesium on the diffusion coefficient of ATP in solutions of physiological ionic strength. *Biochimica et biophysica acta* 1996;**1291**(2):115–121.

89 Dix JA, Verkman AS. Crowding effects on diffusion in solutions and cells. *Annu Rev Biophys* 2008;**37**(1):247–263.

90 Vendelin M, Birkedal R. Anisotropic diffusion of fluorescently labeled ATP in rat cardiomyocytes determined by raster image correlation spectroscopy. *American journal of physiology. Cell physiology* 2008;**295**(5):C1302–C1315.

91 Smith GD, Pearson JE, Keizer JE. in *Computational Cell Biology*eds Fall C P., Marland E S., Wagner J M., Tyson J J. 198–229 Springer: New York 2002.

92 Lambrecht G, et al. Structure-activity relationships of suramin and pyridoxal-5'-phosphate derivatives as P2 receptor antagonists. *Curr Pharm Des* 2002;**8**(26):2371–2399.

93 Charlton SJ, et al. PPADS and suramin as antagonists at cloned P2Y- and P2U-purinoceptors. *Br J Pharmacol* 1996;**118**(3):704–710.

94 Robaye B, Boeynaems JM, Communi D. Slow desensitization of the human P2Y6 receptor. *Eur J Pharmacol* 1997;**329**(2–3):231–236.

95 Marteau F, et al. Pharmacological characterization of the human P2Y13 receptor. *Mol Pharmacol* 2003;**64**(1):104–112.

96 Braun M, Lelieur K, Kietzmann M. Purinergic substances promote murine keratinocyte proliferation and enhance impaired wound healing in mice. *Wound Repair Regen* 2006;**14**(2):152–161.

97 Buckley C, Zhang X, Wilson C, McCarron JG. Carbenoxolone and 18β-glycyrrhetinic acid inhibit inositol 1, 4, 5-trisphosphate-mediated endothelial cell calcium signalling and depolarise mitochondria. 2020.

98 Denning MF, et al. Specific protein kinase C isozymes mediate the induction of keratinocyte differentiation markers by calcium. *Cell growth & differentiation : the molecular biology journal of the American Association for Cancer Research* 1995;**6**:149–157.

99 Ryu SH, et al. Feedback regulation of phospholipase C-beta by protein kinase C. *J Biol Chem* 1990;**265**(29):17941–17945.

100 Yue C, Ku CY, Liu M, Simon MI, Sanborn BM. Molecular mechanism of the inhibition of phospholipase C beta 3 by protein kinase C. *J Biol Chem* 2000;**275**(39):30220–30225.

101 Hofer T, Politi A, Heinrich R. Intercellular Ca2+ wave propagation through gap-junctional Ca2+ diffusion: a theoretical study. *Biophys J* 2001;**80**(1):75–87.

102 Edwards JR, Gibson WG. A model for Ca2+ waves in networks of glial cells incorporating both intercellular and extracellular communication pathways. *J Theor Biol* 2010;**263**(1):45–58.

103 Sneyd J, Wetton BT, Charles AC, Sanderson MJ. Intercellular calcium waves mediated by diffusion of inositol trisphosphate: a two-dimensional model. *American Journal of Physiology-Cell Physiology* 1995;**268**(6):C1537–C1545.

104 Rocheleau JV, Walker GM, Head WS, McGuinness OP, Piston DW. Microfluidic glucose stimulation reveals limited coordination of intracellular Ca2+ activity oscillations in pancreatic islets. *Proc Natl Acad Sci* 2004;**101**(35):12899–12903.

105 Benninger RK, Zhang M, Head WS, Satin LS, Piston DW. Gap junction coupling and calcium waves in the pancreatic islet. *Biophys J* 2008;**95**(11):5048–5061.

106 Pedersen MG, Sorensen MP. Wave-block due to a threshold gradient underlies limited coordination in pancreatic islets. *J Biol Phys* 2008;**34**(3–4):425–432.
107 Bulai IM, Pedersen MG. Stopping waves: geometric analysis of coupled bursters in an asymmetric excitation field. *Nonlinear Dyn* 2019;**96**(3):1927–1937.
108 Keener JP. Propagation and its failure in coupled systems of discrete excitable cells. *SIAM J Appl Math* 1987;**47**(3):556–572.
109 Keener JP. The effects of discrete gap junction coupling on propagation in myocardium. *J Theor Biol* 1991;**148**(1):49–82.
110 Pedersen MG. Homogenization of heterogeneously coupled bistable ODE's-applied to excitation waves in pancreatic islets of langerhans. *J Biol Phys* 2004;**30**(3):285–303.
111 Cappon G, Pedersen MG. Heterogeneity and nearest-neighbor coupling can explain small-worldness and wave properties in pancreatic islets. *Chaos* 2016;**26**(5):053103.
112 Anselmi F, et al. ATP release through connexin hemichannels and gap junction transfer of second messengers propagate Ca2+ signals across the inner ear. *Proc Natl Acad Sci* 2008;**105**(48):18770–18775.
113 Majumder P, et al. ATP-mediated cell-cell signaling in the organ of Corti: the role of connexin channels. *Purinergic Signal* 2010;**6**(2):167–187.
114 Rodriguez L, et al. Reduced phosphatidylinositol 4,5-bisphosphate synthesis impairs inner ear Ca2+ signaling and high-frequency hearing acquisition. *Proc Natl Acad Sci* 2012;**109**(35):14013–14018.
115 Abbracchio MP, Burnstock G. Purinergic signalling: pathophysiological roles. *Jpn J Pharmacol* 1998;**78**:113–145.
116 Neary JT, et al. Mitogenic signaling by ATP/P2Y purinergic receptors in astrocytes: involvement of a calcium-independent protein kinase C, extracellular signal-regulated protein kinase pathway distinct from the phosphatidylinositol-specific phospholipase C/calcium pathway. *The Journal of Neuroscience* 1999;**19**(11):4211–4220.
117 Klepeis VE, Weinger I, Kaczmarek E, Trinkaus-Randall V. P2Y receptors play a critical role in epithelial cell communication and migration. *J Cell Biochem* 2004;**93**(6):1115–1133.
118 Rauhala L, et al. Extracellular ATP activates hyaluronan synthase 2 (HAS2) in epidermal keratinocytes via P2Y2, Ca(2+) signaling, and MAPK pathways. *Biochem J* 2018;**475**(10):1755–1772.
119 Tammi R, Pasonen-Seppänen S, Kolehmainen E, Tammi M. Hyaluronan synthase induction and hyaluronan accumulation in mouse epidermis following skin injury. *J Invest Dermatol* 2005;**124**(5):898–905.
120 Hato T, Dagher PC. How the innate immune system senses trouble and causes trouble. *Clinical Journal of the American Society of Nephrology* 2015;**10**(8):1459.
121 Lovaszi M, Branco Haas C, Antonioli L, Pacher P, Hasko G. The role of P2Y receptors in regulating immunity and metabolism. *Biochem Pharmacol*, 2021;**187**:114419.
122 Collin M, Milne P. Langerhans cell origin and regulation. *Curr Opin Hematol* 2016;**23**(1):28–35.
123 Granstein RD, et al. Augmentation of cutaneous immune responses by ATP gamma S: purinergic agonists define a novel class of immunologic adjuvants. *J Immunol* 2005;**174**(12):7725–7731.
124 Werner S, Krieg T, Smola H. Keratinocyte-fibroblast interactions in wound healing. *J Invest Dermatol* 2007;**127**(5):998–1008.
125 Rodrigues M, Kosaric N, Bonham CA, Gurtner GC. Wound healing: a cellular perspective. *Physiol Rev* 2019;**99**(1):665–706.
126 Jin H, et al. P2Y2 R activation by nucleotides promotes skin wound-healing process. *Exp Dermatol* 2014;**23**(7):480–485.
127 Elsholz F, Harteneck C, Muller W, Friedland K. Calcium–a central regulator of keratinocyte differentiation in health and disease. *European journal of dermatology : EJD* 2014;**24**:650–661.
128 Pellegatti P, Falzoni S, Pinton P, Rizzuto R, Di Virgilio F. A novel recombinant plasma membrane-targeted luciferase reveals a new pathway for ATP secretion. *Mol Biol Cell* 2005;**16**(8):3659–3665.
129 Chen TW, et al. Ultrasensitive fluorescent proteins for imaging neuronal activity. *Nature* 2013;**499**(7458):295–300.
130 Greenberg DS, Kay-Michael Voit DJW, Wuertenberger S, et al. Accurate action potential inference from a calcium sensor protein through biophysical modeling. *bioRxiv preprint*, 2018;1–84. doi:10.1101/479055.